Phyllotaxis as geometric canalization during plant development

Christophe Godin, Christophe Golé, Stéphane Douady

To cite this version:

Christophe Godin, Christophe Golé, Stéphane Douady. Phyllotaxis as geometric canalization during plant development. Development (Cambridge, England), 2020, 147 (19), pp.1-45. 10.1242/dev.165878 . hal-03014239

HAL Id: hal-03014239
https://hal.science/hal-03014239v1

Submitted on 19 Nov 2020

Phyllotaxis as geometric canalization during plant development

Christophe Godin[1,*], Christophe Golé[2], Stéphane Douady[3]

[1]Laboratoire Reproduction et Développement des Plantes, Univ Lyon, ENS de Lyon, UCB Lyon 1, CNRS, INRAE, Inria, Lyon, France
[2]Department of Mathematics, Smith College, Northampton, MA 01063, US
[3]Laboratoire MSC, UMR 7057 Université Paris Diderot – CNRS, Bâtiment Condorcet, CC 7057, 10 rue Alice Domon et Léonie Duquet, 75013 Paris, France
*Corresponding author: christophe.godin@inria.fr

Summary

Why living forms develop in a relatively robust manner, despite various sources of internal or external variability, is a fundamental question in developmental biology. Part of the answer relies on the notion of developmental constraints: at any stage of ontogenesis, morphogenetic processes are constrained to operate within the context of the current organism being built. One universal such constraint is the shape of the organism itself which progressively channels the development of the organism toward its final shape. Here, we illustrate this notion with plants, where strikingly symmetric patterns (phyllotaxis) are formed by lateral organs. This Hypothesis article aims first, to provide an accessible overview of phyllotaxis and second, to argue that the canalization of spiral patterns in plants emerges from local interactions of nascent organs. The relative uniformity of the organogenesis process across all plants then explains the prevalence of certain patterns in plants, i.e. Fibonacci phyllotaxis.

Introduction

Throughout development, morphogenetic processes are constrained by the chemical and physical states of the organism (Alberch 1982, 1991), which biases or limits phenotype variability (Maynard Smith et al. 1985). These developmental constraints progressively restrict the set of possible shapes that can be achieved by the organism, which may orient development in narrow regions of the morphospace. Such canalization of shapes during ontogenesis is believed to be one important source of shape reproducibility in both animals and plants, by making development of shapes largely insensitive to genetic or environmental variations of moderate amplitudes (Wagner 2005, Debat and Le Rouzic 2019)(Supplementary information, section 1).

The spiral arrangement of organs on plant stems, called phyllotaxis, is a striking example of phenotypic bias in development. In spiral phyllotaxis, plant organs form conspicuous spirals, the numbers of which are, surprisingly, usually terms of the Fibonacci's sequence (Box 1). This phenomenon suggests that, during growth, genetic or physical mechanisms are constraining the system to produce specific numbers of spirals, a phenomenon sometimes referred to as "numerical canalization" (Battjes et al. 1993). Interestingly, not only spiral number seems to be canalized, but also the angle between two consecutive organs on the stem, called the divergence angle, which is close to the golden angle (~137.5°) for a vast majority of measurable spiral phyllotaxis (Box 1).

Various conceptual and computational models have been used to study the properties of spiral phyllotaxis (reviewed in Douady and Couder 1996a,b, Adler et al., 1997). Some models assume a constant divergence angle, and derive from this the fact that spiral numbers must be in the Fibonacci sequence (Bravais and Bravais 1837, Hirmer 1931, Fowler et al. 1989, Battjes et al. 1993).

Others make assumptions on the organ initiation process itself, and show that both a constant divergence angle close to the golden angle and Fibonacci spirals may emerge from the dynamic interaction between recently created organs (Schwendener 1868, Douady and Couder 1996a and b, Atela et. al, 2003). Before technology became available to observe the actual molecular or physical actors governing phyllotaxis patterns, early studies suggested the existence of abstract mechanisms that could produce phyllotaxis patterns at a macroscopic level and studied their theoretical properties. However, a clear picture of what exactly governs the canalization of patterns during plant growth remains elusive.

Here, our aim is twofold. As it is difficult for the non-specialists to easily grasp the essence of phyllotaxis models, our first objective is to give an articulate, concise and accessible introduction to the key concepts related to the analysis and modeling of spiral phyllotaxis patterns. We focus on the geometric explanations that are central to the understanding, abstracted from molecular or physical mechanisms while keeping the mathematics light. Our second aim is to investigate the nature of the process(es) that canalize phyllotaxis patterns so efficiently. The Fibonacci property of spiral patterns observed in plants is suggested to result from developmental constraints (Maynard Smith et al. 1985) imposed by the close packing of organs at the tip of growing stems (Mitchison, 1977), but how is the divergence angle canalized? Are both Fibonacci properties and divergence angle canalizations related? To address these questions, we show how robust and conspicuous spiral phyllotaxis patterns are channeled by purely geometric developmental constraints throughout plant development, and we provide a detailed account of the origin of these constraints.

Overall, we propose that a coherent view emerges from the collective effort to understand phyllotaxis, in which the competition of organs for space in the shoot apical meristem (SAM), imposes simple, local and robust geometric rules for the ring of newly formed organs around the SAM (front). As growth accelerates during development, the shape of the front formed by the previous organs constrains increasingly accurately the position of the next ones, and geometrically channels the phyllotaxis into a very restricted number of patterns. This mechanism can explain both the universal presence of Fibonacci phyllotaxis in plant patterns and its exceptions (depending on the variation of the growth rate), suggesting that phyllotaxis patterns are continuously canalized during plant development by purely local geometric constraints.

Spiral phyllotaxis patterns

Phyllotaxis patterns are usually classified into either spiral (Fig. 1A) or whorled (Fig. 1B) motifs according to the number of lateral organs attached at each node. In the large class of spiral phyllotaxis on which we focus in most of this paper, the patterns are usually described by two families of visual spirals: the parastichies (Fig. 1C). In the early 19th century (Braun 1831), it was recognized that the numbers of spirals of these clockwise and counterclockwise parastichies are, generally, two consecutive numbers of the Fibonacci sequence, called the *phyllotaxis mode* (Box 2; Fig. 1D,E). Unusually for biological systems, these spiral numbers only deviate marginally from this rule (around a few percents)(Fierz 2015, Swinton et al. 2016), suggesting strong, relatively universal developmental constraints (Maynard Smith et al. 1985).

The lateral organs composing these patterns are produced by the SAM (Fig. 1F) at a regular pace at the tip of plant axes around the rim of a central zone (CZ). The organs and stem then grow and expand to reach their final size and shape, during which they generally keep their relative angular positions on the stem. The angle between two consecutive organ primordia is called the “divergence angle” (Schimper 1835)(Fig. 1G,H). In most plants, this angle does not change as the primordia develop into mature organs. Divergence angles may either be relatively constant during some growth phase of the stem or show gradual variations. The imaginary curve linking the organs at consecutive nodes of a given stem (in the order of their initiation) is called the “generative helix” or “generative spiral" (Fig. 1H) if the organs mainly stay in one plane. This spiral winds either to the left or to the right (chirality).

On elongated stems, the divergence angle can be easily estimated by computing its average value from the number of turns and organs separating two overlaying leaves (Fig. 1H) on the generative helix (Schimper, 1835). Similar estimations are difficult in compact structures, such as flowers or cones, because one cannot easily see the organs' order between overlaying leaves. Rather, these compact structures show "contact-parastichies": generally, organs do not exactly overlay and, if the structure remains compact, one can observe a corresponding slight shift on one side (Fig. 1I). During development, this shift always occurs in the same direction, which creates the "contact-parastichies" due to the visual adjacency between organs (Fig. 1J). These visual spirals must not be confused with the generative spiral that can be seen as the most horizontal possible spiral winding around the stem and which traverses each organ in their chronological order. For spiral phyllotaxis, the average divergence angle (when it can be measured) is usually close to the golden angle (137.5°) (Box 1; Fig 1G). Less frequently, other angles such as 99.5° (Lucas angle) can be found (Fierz 2015, Swinton et al. 2016). Remarkably, both the golden angle and Lucas angle are tightly connected with the Fibonacci sequence (Box 1), supporting the intuition that something profound connects these botanical patterns – and their resilience to internal, environmental and genetic variations – to mathematics.

Thus, numbers of parastichies and divergence angles both seem to be constrained, taking their values within restricted ranges. Where do these developmental constraints come from? Do they reflect a single underlying mechanism, acting on the parastichy numbers, or the divergence angle? Or are two different mechanisms at play?

The geometric link between divergence angle and spirals

To better understand the intricate relationship between divergence angle and parastichies, consider a toy geometric model of organ initiation (Fig. 2A, (Golé 2020)). In this toy model, organs form, one at a time, at the rim of the meristem CZ of radius R. The time elapsed between two consecutive organ initiations (T) is called a "plastochron", and the azimuthal angle (α) between these organs defines the divergence angle. As organs are produced, they immediately move radially away from the center with a constant velocity V. For simplicity, we assume that apex growth is regular (stationary growth), so that V, T and α, are considered as independent and constant parameters (Box 2). In addition, we measure angles as fractions of a circle: any angle is represented by a real number between 0 and 1 (the angle unit is a turn: 1 turn=360°, 1/2 turn=180°, 1/3 turn = 120°, etc. (Box 1)).

Connecting divergence angles and spiral motifs

Using this model we can simulate the growth of an imaginary apex during a given number of plastochrons. First, observe what happens when varying the divergence angle α (α stays constant during each simulation, but is distinct between two simulations), while R=1 and V=1 in arbitrary units (a.u.) are fixed between all simulations. For α=1/2, the model generates two opposite straight arms at 180° of one another (Fig. 2B). The primordia are generated alternatively on each side and move away from the center, thus leaving room for the next primordium on the same side every two plastochrons. The two arms are thus composed of even and odd primordia, respectively, and form "opposite phyllotaxis", commonly observed in plants. Setting α=1/3, yields three emerging straight arms. Likewise, for α=1/4, four straight arms emerge and so on (Fig. 2B).

Both α=1/5 and α=2/5 appear to have five arms (Fig. 2C). However, the order in which the arms are visited differs. For α=1/5, the arms are visited in the order 1,2,3,4,5, but in the order 1,3,5,2,4 for α=2/5 (Fig. 2C, green arrows). The numerator p indicates the number of turns that are made before the organ initiation occurs again in the initial orientation (i.e. on arm one). Equivalently, it also indicates the number of arms that are skipped from one initiation to the next during the simulated growth process. For example, α=3/7 yields a motif with seven straight arms that are all visited every three turns before the simulation comes back to the original azimuth angle for initiating an organ, α=5/12 yields twelve arms, etc.

Shall we then conclude that if the divergence angle is defined by a fraction p/q of a turn, then the motif always exhibits q straight arms? Not quite. Consider what occurs by slightly changing the value of a divergence angle in the previous simulations, for example, α=0.401 instead of α=2/5=0.40. Note that this new divergence angle is also rational, as 0.401 = 401/1000. Shall we expect a motif with 1000 straight arms? We do not observe this (Fig. 2D). Instead, the previous five arms for α=2/5 are now slightly bending. By increasing the divergence angle to α=0.41, the five arms bend even more. However, for α=3/7, the five bending arms disappear and are replaced by seven straight arms, as previously observed. For α=0.43, the seven arms bend again. However, both 0.41=41/100 and 0.43=43/100 are rationals. Why don't we see 100 straight arms?

A different way to bend arms

For a solution, consider a different way to bend the arms of our phyllotaxis motifs. Instead of changing the divergence angle, let us keep it constant (α=0.41), as well as V=1 and R=1, and change the time T between the initiation of two organs between simulations (Fig. 2E). For T=0.1, we observe five spiraling arms, coiling clockwise away from the center. A 2-fold decrease (T=0.05) increases the bending of the five arms. Indeed, decreasing T progressively coils the arms tighter around the center; the angular positions of the points don't change, but their distance to the origin decreases, bringing points in the different arms closer together, so much so that the eye wants to connect newly neighboring points into new spirals. For T=0.05, for instance, one can perceive, aside from the five original spirals, a new set of 17 spirals coiling counterclockwise from the origin. We say that the pattern is in a (5, 17) mode (Box 2), or that its number of parastichies are (5, 17)(Fig. 2E). At T=0.01, one can still perceive the five clockwise and 17 counterclockwise spirals close to the center, in a much tighter coil. However, on the outside, two more sets of spirals have emerged: one with 22 clockwise spirals, the other with 39 counterclockwise spirals. This presents a transition of modes, common to asteracea's flower heads (Supplementary information, section 2). Note that, the more spirals in one of these sets, the straighter the spirals: the 5-spirals are most coiled, the 39 are the least. For T=0.001, α=41/100, all these spirals have coiled so much that the only pattern visible is -long expected- 100 equally spaced straight arms shooting radially from the center.

It is important to note that, in these toy-simulations, we have kept the parameters R and V constant, and varied only the plastochron T and divergence angle α independently. We could have obtained the same result by keeping constant the plastochron T=1 arbitrary unit, and varying the speed V of primordia drift instead. What actually matters for the patterns is not each individual parameter but their product VT that corresponds to the distance travelled by one primordium during one plastochron. This defines a typical length scale that must be compared with the size of the apex, i.e. the radius R of the CZ. The patterning is thus governed by the ratio, $G=VT/R$, between these two spatial quantities that characterizes the apex growth. This "growth index" (G) can be measured directly from cuts or electron microscope pictures, even without scale, from the respective distance of the organs (Richards 1951). Thus, we now use the two variables: α, G (instead of α, T), where G can be varied by changing the value of either T, V or R.

For a given divergence angle, the number of arms generally depends on the growth index G, (Fig. 2E). As we have seen, decreasing G increases the number of arms. But why do we eventually see 100 straight arms for $\alpha = \frac{41}{100}$? How can we explain the numbers of spirals (5, 17, 22, 39) that we saw on our way to 100?

The numbers of spiral arms correspond to best rational approximations of the divergence angle at different resolutions

To understand this, let us consider more closely the numerical structure of our divergence angle α=0.41. We make use of the fact that each real number can be increasingly well approximated by a unique series of fractional (rational) numbers called its "convergents" (Box 3, Supplementary information, section 3). For instance, 41/100 can be increasingly well approximated by the sequence of rational numbers:

$$\left[\frac{1}{2}, \frac{2}{5}, \frac{7}{17}, \frac{9}{22}, \frac{16}{39}, \frac{41}{100}\right]$$

which, respectively, correspond to:

0.5, 0.4, 0.4117…, 0.40909…,0.41025…,0.41

Each fraction *p/q* in this list is the best rational approximation of 0.41 that one can make with pieces of size 1/*q* or larger (Box 3 and Supplementary information Section 3, as well as e.g. (Karpenkov 2013) for mathematical details). For example, 7/17 is the best rational approximation that one can make of 0.41 with pieces of size 1/17 or larger (i.e. it is a convergent of 41/100), (Fig. 3A)).

How do these convergents appear in the geometry of our spirals? We have seen before that, for some range of growth index, when the divergence α is close to a rational *p/q*, the pattern displays *q* arms, and these arms become straighter as α moves closer to *p/q*. So seeing the successions of 5, 17, 22, 39 and finally 100 arms at different growth indexes is just the expression of the fact that 41/100 is successively close to its convergents (Box 2). As *G* decreases, the pairs of spirals coil onto themselves (Fig. 2E). During this process, for a given mode, spirals that are the least tightly wound, corresponding to the convergents with higher denominators, and whose points are farther apart (Fig. 3A, 17 purple spirals), become increasingly visible. By contrast, the most tightly coiled spirals of the pair (Fig. 3A, five green spirals) tend to coil even more and to disappear in the tight packing of organs as *G* continues to decrease (Fig. 2E). This process leads to progressively exhibiting pairs of spiral families, alternatively clockwise and counterclockwise, whose numbers run successively through the list of denominators of the convergents of α (Fig. 3A).

When the divergence angle is the golden angle, the number of visible spirals are consecutive numbers of the Fibonacci sequence

In the previous sections, we considered exclusively rational divergence angles. However, all the previous conclusions remain valid for irrational numbers: a unique list of convergents can be defined that gives a multiresolution approximation of this number (Supplementary information, section 3).

What about the Golden angle? In 1830, Schimper and Braun (Schimper 1835, Braun 1831) made the first observations of Fibonacci phyllotaxis. They defined the divergence angle and hypothesized that, given their observations, most often it must belong to a sequence of rationals formed by quotients of numbers that are two apart in the Fibonacci sequence (Box 1). Independently, the Bravais brothers (Bravais and Bravais 1837) made similar observations, except that they always saw bending arms (or, on a stem, skewed vertical rows of organs) (Supplementary information, section 2; Fig. 1J). They realized that these numbers are actually the first terms in the list of convergents of the golden angle $\gamma = \frac{1}{\phi^2}$ (Supplementary information, section 4). Note that, although the Bravais brothers remark that γ is irrational – explaining the bending of arms at every scale – they make no mention of its relation to the golden ratio, whose relation to the Fibonacci number was not as widely known as today.

According to what we discussed above, the number of spirals that are observed in motifs corresponding to an angle of divergence γ must be consecutive denominators of its sequence of convergents, that is the fractions $\frac{1}{2}, \frac{1}{3}, \frac{2}{5}, \frac{3}{8}, \frac{5}{13} \cdots$ whose limit is γ (Fig. 3B, Supplementary information, section 4), i.e. the number of parastichies must be pairs of consecutive Fibonacci numbers.

Must all plants with Fibonacci phyllotaxis have constant divergence angle γ? This is the hypothesis that the Bravais made. Here was one number that could explain the vast majority of the plant patterns they observed, and whose average divergence angle they measured seemed to be very close to γ. This hypothesis persisted as a diktat for nearly 200 years. Yet, the Bravais (Bravais and Bravais 1837, p.73) warn us that this might only be a guiding hypothesis (our translation): *"Let us note once more that we are not pretending to prove in a rigorous manner that the divergence angle is constant, but we deem it as the most likely hypothesis in our present state of knowledge; were it only a theoretical idea to verify, it would still be a useful guide in the study of plant symmetry, or Phyllotaxis, as Mr. Schimper calls it."*

Summary

This section has shown that, via a simple regular spiral model, there is a strong, but subtle, mathematical link between divergence angles and parastichies. Spiral patterns are simply geometric representations of the fixed divergence angle with varying precision levels that are determined by the growth index *G*. Straight arms indicate that the organs move sufficiently slowly away from the center so that their positions provide an exact estimation of the divergence angle (when rational). In contrast, bending arms reveal that the growth index is too large for straight arms to be visually perceptible (as one would expect for a rational divergence angle), or alternatively, that the divergence angle is irrational. Instead, visible arms correspond to best approximations of the divergence angle. Note that, due to this property, bending arms can appear even for rational divergence angles.

Depending on divergence angle and growth index values, one or two spiral families can be observed (Fig. 2D,E). Reciprocally, the numbers of clockwise and counterclockwise spirals inform us of the possible underlying divergence angle (assumed to be constant in this idealized situation), sometimes referred to as the fundamental theorem of phyllotaxis (Bravais and Bravais 1837, Adler 1974, Jean 1986) (Box 4, Supplementary information, section 5).

The toy geometric model assumes that growth index and divergence angle are independent variables and have constant values. If the divergence angle is set to the golden angle, classical families of Fibonacci spirals become visible. However, many other phyllotaxis modes can be observed for other values of the divergence angle, whether it be in nature (where they are less frequent) or in simulations.

Fibonacci modes are predominant in plants with spiral phyllotaxis, suggesting that something else is probably constraining the system. In principle, either the divergence angle or the parastichies could be constrained by the growth processes to take precise values, consequently restricting the range of values taken by the other through the geometrical link described above. However, both cases raise interpretation difficulties: if developmental constraints act directly on spirals, selecting specific numbers of arms, how are these numbers consecutive numbers of the Fibonacci sequence? Conversely, if developmental constraints directly regulate the value of the divergence angles, why is this value is most of the time close to the golden angle? Even for divergence angles deviating slightly from the golden angle (α=136, 137, 138, etc.), we observe spiral patterns showing large gaps between parastichies and modes unobserved in plants (Prusinkiewicz and Lindenmayer 1990)(Fig. 3C). If the divergence angle were indeed constant and equal to the golden angle, how could the plant maintain precision, such that only Fibonacci spirals are observed macroscopically? And why could other divergence angles be seen occasionally, while often showing parastichy numbers related to the Fibonacci sequence in those cases (e.g. Lucas angle = 99°5)? These paradoxes are partly resolved because the divergence angle and the growth index are *not* independent variables in real plants.

The coupling between growth index and divergence angle

In the previous simple geometric model, we were interested in the positions of primordia without considering their actual size nor their physical or chemical interactions. However, in meristems, young primordia may encompass a tissue region of several cells of diameter and inhibit the initiation of other organs in their immediate vicinity. Each primordium defines a zone of exclusion around it, where no other organ can form, which seems to be mainly determined molecularly (Reinhardt et al. 2003, Barbier de Reuille et al. 2006, Smith et al. 2006, Jönsson et al. 2006, Besnard et al. 2014, see the Biological Interpretation section below)), although a physical (mechanical) contribution cannot be excluded (Galvan Ampudia et al. 2016). Here, we identify the primordium region and the inhibition zone around it as the "primordium" as a whole, without paying attention to distinction between the primordium proper and its lateral inhibition nor to the exact nature of the inhibition, which are not essential to this discussion.

Toward a more mechanistic model taking into account organ contacts

Many mechanistic models take into account such inhibitory action between organs at the meristem. The most common view is that primordia are initiated at the rim of the CZ, which is crowded by young primordia (Fig. 1F; Fig. 4A). By their local inhibitory action, these primordia inhibit the formation of new primordia, provided they keep close enough to the CZ. However, due to growth, the CZ drifts away from the existing primordia and new primordia can form as soon as sufficient space is available. This process results in "contacts" between primordia at the edge of their individual inhibitory zones (Hofmeister 1868). These contacts reflect the geometry of zones of inhibition, be they due to physical contact or chemical signal. With growth, this contact pattern is often preserved in compact structures (Fig. 4C) and remains visible in elongated stems with the vasculature (Plantefol 1948, Kirchoff, 1984). Altogether, the prevalent hypotheses governing local interactions between organs at the tip of growing meristems are:

i. *Circular symmetry*: The meristem can be approximated by a surface of revolution (disk, cone, cylinder...);

ii. *Center inhibition*: no organ can form in the CZ of the circular meristem;

iii. *Primordia inhibition*: young primordia inhibit the formation of new adjacent organs;

iv. *Tissue growth*: previously formed primordia are left behind the growing tip, or equivalently they are seen moving radially away from the initiation zone at the tip of the SAM. The primordia themselves grow in size keeping their original contacts;

v. *Deterministic initiation*: primordia form at the edge of the CZ when and where overall inhibition is sufficiently low, thus establishing initial close packing with the previous primordia.

Many phyllotaxis morphogenesis models imply, more or less explicitly, these five major assumptions (Schwendener 1878, Snow and Snow 1952, Veen 1973, Mitchison 1977, Douady and Couder 1996a,b,c, Atela et al. 2003, Smith and Prusinkiewicz 2006, Pennybacker et al. 2015). In the simplest (and oldest) instance of these models (Schwendener 1878), the geometry of meristems is abstracted as a packing of circular organs (Fig. 4B), for which "contact" parastichies can be identified by joining each primordium to its two *older contact neighbors* (Box 2). Depending on whether one concentrates on the top, so-called "centric" view of the meristem (Fig. 4A,B) or on a "cylindrical" view (Fig. 4C,D) the underlying geometry is either approximated by a planar annulus or a cylinder, respectively, which can be put into a one-to-one mathematical correspondence (Supplementary information, section 2). Given this correspondence, the geometric assumptions that follow are not overly simplistic.

We thus represent the region around the meristem of diameter D by a cylinder which, unrolled, turns into a rectangle of width $C=\pi D$, the circumference of the CZ. The upper boundary corresponds to the rim of the CZ and the primordia are represented as disks with identical (for now) diameter d on the surface of the cylinder (Fig. 4B). As the geometry of this system is preserved for identical ratios d/C up to a scaling factor, we conveniently set the CZ circumference C=1 in our model, meaning that d should be considered as the ratio of the primordium diameter over the diameter of the CZ. In this cylindrical representation, angles between two primordia are represented by the horizontal distance between their centers with values between 0 and 1: as before, we choose the unit of angle to be a turn. Likewise, assuming as before that the displacement velocity V=1, the vertical distances between successive primordia centers, corresponding as before to the growth index G, can be thought also as the time lag that separates their initiation (plastochron). Divergence angles α are thus represented by the horizontal component of the vector between pairs of consecutively initiated primordia, while growth indices G correspond to their vertical components.

Using this cylindrical representation, we can upgrade the previous descriptive toy model and make use of a mechanism of pattern formation: our five rules come down to the simple disk stacking model, initially introduced by (Schwendener 1878). In this model, *disks are stacked one by one on the surface of the cylinder in the lowest possible place above the previous disks, without overlap.* Given a rate of growth, both the plastochron and the divergence can be read from the vertical and horizontal displacement between the new disk and the previous one. This reflects hypothesis (v) above: primordia form when and where inhibition is sufficiently low, i.e. when and where there is enough space. Regularity of the divergence and plastochron over the longer run, when it happens, is then an emergent consequence of this fundamentally local mechanism.

Contrary to the earlier geometric model, this model enforces contact between every new primordium and at least two older neighbors located on opposite sides of it. This contact constraint, which can be seen as a local spatial optimization by the plant morphogenesis, drastically reduces the space of possible observable pairs (α, G) and is at the origin of phyllotaxis as a self-organizing process.

Coupling of growth index and divergence: the van Iterson diagram.

To understand how taking into account the contacts between primordia reduces pattern possibilities, let us use our simple contact model and stack disks of constant diameter d on the cylinder while keeping α and G constant. For each value of the pair (α, G), this process produces a regular motif (Fig. 4B,D). Joining nearest neighbors gives rise to two (sometimes three) sets of parallel straight lines (i.e. the parastichies). These straight lines crisscross the unrolled stem cylinder into a *lattice motif.* For that reason, these regular disk patterns are called *cylindrical lattices*, or lattices for short (Fig. 4E(a–d), and Box 2.). Note that, rolled back on the cylinder, the straight parastichies are helices.

If, as in our first toy geometric model, the contact constraints are not taken into account, α and G can take any value independently. Each pair (α, G) gives rise to a particular lattice motif made of two (or three) families of parastichies. The number of parastichies in each family (the *mode* of the lattice as for the previous toy model) can be nicely read off the index of the two disks closest to the reference Disk 0 (Braun 1831): if the closest disks are Disks 8 and 13 for instance, there must be 8 parastichies parallel to the one through Disks 0 and 8 (Fig. 4D, red lines). Likewise, there are 13 parastichies parallel to the one through Disks 0 and 13 (Fig. 4D, green lines). So, the parastichy numbers, or mode, are (8, 13) here. They are also easily counted in the corresponding centric view (Fig. 4B).

Each pair (α, G) thus corresponds to a lattice with a specific mode *(i, j)*. Let us associate a unique color with each different mode *(i, j)* and color each point of the α, G-plane with the color of its corresponding lattice's mode. This produces colored "*(i, j)*-regions" that form a beautiful fractal pattern (Fig. 4E). These regions have different sizes and are separated by arcs of circles, with the smaller regions, of higher modes, accumulating down near the α-axis (Supplementary information, section 5). This makes sense since a smaller G corresponds to smaller d or, equivalently, to a larger stem diameter (i.e. a later stage of development).

However, as discussed above, in the more realistic contact model, primordia are formed in contact with existing ones. Therefore, not all pairs of points (α, G) realistically represent plant patterns. Indeed, in plants, each disk (primordium) has two older contact neighbors below it, which must be its closest neighbors. Thus, in this case, all parastichies connect contacting disks (contact parastichies, Box 2). Lattices formed with that contact property are called *rhombic lattices* (Box 2), because the segments joining contacting disk centers all have the same length d and thus the parastichies partition the cylinder into identical rhombic tiles (Atela and Golé 2007)(Fig. 4D). Imposing the contacts of the disks also links the parameters d/C and the growth index G (or the plastochron) as $G \sim (d/C)^2$ when contacts are assumed (van Iterson 1907, Douady 1998)(Supplementary information, section 2).

Moving in the α, G-plane while keeping the disks of the corresponding lattice in contact strongly constrains the possible moves (the reader can dynamically experiment these constraints with the online geogebra app (Golé et al. 2020)). Van Iterson (1907) realized that such constraints impose moving along a tree-like structure embedded in the α, G-plane. To show this, he expressed the constraint for lattices to be rhombic as quadratic equations in α and G. In the α, G-plane, these equations represent arcs of circles arranged like branches of an upside-down tree-like figure (black curves in Fig. 4E), each branch, that we call *(i,j)*-branch, traversing a unique *(i,j)*-region (Supplementary information, section 5). Van Iterson drew a remarkably precise representation of this tree, suggestive of its fractal nature, which is now called the van Iterson Diagram. Each point in the tree represents a value of α and G giving rise to a rhombic lattice, compatible with the stacking process. Note that most points in the α, G-plane are outside the tree and give rise to lattices that are not rhombic (e.g. the lattice in Fig. 4E(a) only has one set of contact parastichies).

Lowering G while making sure that the corresponding lattice remains rhombic, the lattice changes mode according to the Fibonacci rule. In Figure 4E, one can see the Fibonacci progression *(i, j)* = (5,3) -> *(i, i+j)*=(5, 8) in the points (b), (c), (d) by paying attention, in the corresponding lattices, to which disks are the older contact neighbors of the newest disk (labeled 0). At the bottom of the branch *(i,j)*, the third disk *i+j* becomes an older contact neighbor (Fig. 4E(c)). Decreasing G further, the older contact neighbors must be *i+j* and the *largest* of *i* and *j*: the other choice yields contact neighbors on the same side of Disk 0, which is not allowed by the stacking process (Fig. 4E(d)). This is exactly the Fibonacci adding rule: *i, j → max(i, j) , i+j*.

In an idealized sense, a developing plant travels down the van Iterson diagram. Monocots or dicots start on a branch of the diagram with low mode, for instance (1,1): the first leaf grows opposite the cotyledon or pair of them, and the next leaf opposite to the first etc. As the meristem grows in girth, while the diameter of the primordia remains roughly constant, the parameter G decreases. Eventually the point (α, G) corresponding to the pattern reaches a fork where the branches *(1, 2) or (2, 1)* meet. In this case, going down on either branch is allowed (this is a choice of chirality in a plant organ). Say the pattern proceeds down the *(2, 1)* branch*.* The next transition is then determined: following the Fibonacci rule, it must be *(2, 3)* (and not *(3, 1)* since contact neighbors must be on opposite sides). From then on, the continuous deformation of rhombic lattices imposed by the decrease of G inexorably yields successive Fibonacci modes. Moreover, the zigzagging curve travelled during this process converges on the α-axis to the golden Angle γ.

While Schwendener (also Adler, 1974) believed that lattice deformation played a role in the pattern formation, van Iterson initiated a paradigm, further developed by many subsequent authors (Veen and Lindenmayer1977, Mitchison 1977, Douady and Couder 1996a and b, Koch et. al 1998, Kunz 1995, Atela et. al. 2003) whereby the dynamical process of pattern formation navigates, as the parameter *G* varies, from a lattice (or close to it, Atela and Golé 2007) to another, along the van Iterson diagram.

This paradigm strongly suggests that the divergence angle is progressively canalized as the plant grows by the allowed van Iterson diagram trajectories towards the golden angle. However, it ignores much. It relies on the assumption that, under the dynamical process, patterns naturally tend to become rhombic lattices, which is only true in restricted circumstances (Atela et. al. 2003). Indeed, in general, the stacking process yields patterns with crooked parastichies, which are not simple lattices (Golé and Douady 2020). Moreover, with few exceptions (van Iterson 1907, Douady and Couder 1996c), works espousing the van Iterson paradigm that patterns evolve from one lattice to another ignore what patterns actually do in between. To focus on these transitions, one needs a more local approach to plant patterns than lattices. However, the van Iterson diagram can remain a subtle, but useful, guide even in such an approach.

Canalization of Fibonacci phyllotaxis via fronts

When considering plant growth dynamics, the phyllotaxis is not actually a sequence of stationary modes, which might not have time to stabilize and have significant transitory phases. A model is required that also accounts for transitions between modes, localized where primordia are formed. A logical approach concentrates on the portion of the phyllotactic pattern most immediately responsible for the future of the pattern, i.e. the most recent layer of primordia directly surrounding the meristem. In the disk stacking model, this corresponds to a "front": the top layer of disks encircling the cylinder (Hotton et al. 2006, Golé et al. 2016)(Supplementary information, section 7). If a new primordium appears as soon as there is enough space, the next disk added to the structure must be in contact with disks of the front, and at the lowest possible position. The history of a pattern can be traced via its successive fronts, represented by a zigzagging curve joining centers of adjacent primordia in the front (Fig. 4A-D).

The numbers of line segments joining adjacent primordia of the front, going up or down as we move along the front (Fig. 4A-D) define the front parastichy numbers. In regular patterns (e.g. lattices), these front parastichy numbers correspond to the usual numbers of parastichies (the mode) of the whole pattern. The true power of the model arises when changing the size of the disks with respect to cylinder size (i.e. changing the parameter d/C). In plants, this occurs when the meristem's diameter *D* grows as the stem matures, while the primordia's diameters remain of roughly equal size *d*.

Let us start with a regular front, i.e. with similar up and similar down segments, and stack disks on it, in the lowest possible place without overlap, while slowly decreasing the size *d* of the disks as they move up (Fig. 5A). The evolution of the front automatically generates a recursive "Fibonacci machine", whereby a front with parastichy numbers (i, j) with, say, $i < j$, evolves, after successive stacking of disks of slowly decreasing size, into another front with parastichy numbers ($i+j, j$), (Fig. 5A,B). This remarkable property of fronts emerges from local "triangle transitions": in general, a new disk appears at the bottom of a notch of a front, forming a rhombus with disks on either side of the notch (Fig. 5B') (Supplementary Information, section 6). In this case there are no changes to the parastichy numbers. When reducing the disk size, however, the angles of the notches in the front open up and it is no longer possible for the new disk to be in contact with disks on opposite sides of a notch. Instead the new disk is in contact with two adjacent disks on the same side of a notch, these three disks now forming a triangle. Each such triangle gives rise to an additional new parastichy (Fig. 5A",B). To find the lowest position, the new disk appears at the flattest side of the notch (Fig. 5B insert). Crucially, to obtain the next Fibonacci parastichy number, one needs enough regularity of the front to fall into the right places and in the right number; the flattest segments must either be all up or all down segments of the front. (Fig. 5A'). When starting with i=1, j=1 or j=2 (many plants do, with one or two cotyledons serving as initial leaves) this recursive mechanism yields the successive Fibonacci modes seen in plants (Fig. 6A,B). Systematic simulations that sweep the parameter plane of possible angle of (1, 1) fronts and rates of decrease of *d*, consistently detect this Fibonacci pattern formation, and its associated front regularity, when *d* (or *d/C*) decreases slowly enough (Fig. 6B', Supplementary information sections 6-7, Fig S9). The mechanism is reversible in a sense: increase *d/C* and the parastichy numbers will decrease, via ordered pentagon transitions, as happens in compositea inflorescence, where the diameter of the CZ decreases as primordia fill up the meristem (Fig. 6C-C');

This model suggests that the regular geometry of the fronts serves as the successive checkpoints in the developmental canalization of the phyllotactic pattern: starting with a regular enough Fibonacci front, the biological stacking-like mechanism of primordia formation predictably yields, if the parameter *d/C* decreases slowly enough, a succession of fronts that retain their regularity. The regularity, in turn, guarantees that in the transitions the parastichy numbers follow the Fibonacci addition rule. Interestingly, the stacking model also predicts that, when *d/C* decreases too quickly, the fronts becomes irregular and the triangle transitions distribute on both the up and down segments of a front, yielding parastichy numbers *i, j* with *i/j* close to, but not necessarily equal to 1. This quasi-symmetric phyllotaxis (Golé et al. 2016) is actually observed in many plant inflorescences such as corn, peace lily, strawberry (Supplementary information, section 7).

The golden angle as an emergent phenomenon

A constant angle of divergence is not required in the front-based explanation of Fibonacci pattern formation; therefore, it is not the driving concept behind phyllotaxis morphogenesis. Is it a by-product then? When looking at the graph of the divergence angle along simulated Fibonacci growth (Fig. 7B) it seems not to be. Indeed, the divergence angle oscillates closer and closer to the golden angle up to 30 iterations, but then it breaks up in large oscillations, even though the pattern itself seems relatively regular (Fig. 6B). Importantly, the angles between which the divergence oscillates are all close to *multiples* of the golden angle (Douady and Couder 1996b, Golé et al. 2016)(Fig. 7C). This explanation becomes clearer when inspecting the order in which the disks appear on the front: as the disks become smaller, small irregularities of the front may induce permutations in the stacking order of these new disks on the front (Fig. 7A', A"). This permutation phenomenon is not an artifact of simulations: it is observed in Magnolia, *Arabidopsis* and Birch catkins (Zagorska-Marek 1994, Besnard et al. 2014, Douady and Golé 2017), and studied in the framework of stochastic processes to account for biological noise in plant molecular processes (Refahi et al. 2016).

Do these wide divergence angle fluctuations invalidate the hypothesis of the golden angle being central to phyllotaxis? Not quite. By taking the mean of the divergence angle over each front, the permutations average out and the regularity of the divergence angle reappears, which closely follows the oscillating convergence to the golden angle along the van Iterson diagram (Fig. 7E, E'). In this precise sense – while it is not its mechanistic principle – the golden angle divergence *is* an emergent by-product of Fibonacci patterning.

Biological interpretation of primordia initiation

In the last two decades, the molecular and physical origins of the concepts used in phyllotaxis models, (e.g. CZ, inhibitory fields, organ initiation threshold, growth or fronts), have been investigated using model plants such as *Arabidopsis thaliana* (Kuhlemeier 2007, Traas 2013, Galvan-Ampudia 2016, Bhatia 2018). Instead of an inhibitor, an activator was found: the accumulation of auxin, (an ubiquitous phyto-hormone,) *induces* organ initiation at the CZ rim (Reinhardt et al. 2003). Auxin, is mainly synthetized in the young organs (Reinhardt et al. 2003, Galvan-Ampudia et al., 2020) and actively transported at the meristem tip, through membrane transporters of the PIN1 family (Reinhardt et al. 2003, Barbier de Reuille et al. 2006, Smith et al. 2006, Jönsson et al. 2006). Local accumulation triggers organ outgrowth, subsequently depleting local auxin, which is equated with the abstract inhibitory fields hypothesized in phyllotactic models: a meristem tip is abundant with auxin, except in the places where young organs have been initiated. The CZ also contains high levels of auxin (Barbier de Reuille 2006, Vernoux et al. 2011, Galvan-Ampudia et al., 2020). However, the CZ remains insensitive to the auxin signal, and no organ can form there (Barbier de Reuille et al. 2006, Vernoux et al. 2011, Ma et al. 2019). The fronts correspond to the spatial variation of auxin concentration along the CZ rim (Fig. 8), that shows creases between existing organs, prefiguring the positions of upcoming initiations (Refahi et al. 2016, Galvan-Ampudia et al., 2020).

This cellular work shows that all the mechanisms are local. The intricate instabilities described explain how a primordium is initiated at some distance of the CZ and of the other primordia, exactly as described by (Hofmeister, 1868). There is no mechanism found that imposes a fixed divergence from a distant previous primordia, reinforcing the vision that phyllotaxis is purely the result of front local dynamics, which canalizes the possible outcomes.

Summary

Organ initiation rules in SAM and fronts provide a simple explanation of the nature of developmental constraints at the origin of spiral phyllotaxis patterns in plants. Contrary to original hypotheses (Bravais and Bravais 1837), developmental constraints apply locally to parastichies, which in turn determine the mean divergence angle (not *vice versa*). This is because all lateral organs in plant stems, be they part of compressed or elongated structures, are initiated in a tiny region at the SAM where competition for space is paramount. There, patterning is dominated by the opportunistic initiation of organs as the initiation zone progressively leaves the already initiated organs, governed by the geometric arrangement of recently initiated organs (the fronts) and by the plant growth (the parameter d/C) and its variations.

During stem growth, phyllotaxis is progressively canalized from a (1, 1) front with divergence angle of 180° (1/2 turn) to higher order Fibonacci fronts with average divergence angles that converge to the golden angle. These features emerge from the inhibition- and growth-based iterative process of primordia formation making transitions from front to front. If the variation is slow enough, and starting from a regular enough front, this localized positioning mechanism leads to a global order – imperfect but robust. This regularity imposes not only the continuation of the pattern, but also the successive addition of the "right" numbers of spirals following the Fibonacci rule at the transitions. The system starting with an angle of 1/2 a turn between the first two primordia, imposes the coarser convergents of the divergence angle: 1/2 then 1/3. Any divergence angle that would have both 1/2 and 1/3 as its first convergents would then be consistent with the pattern. The precise angle is determined by the rate of decrease of the organ size relative to the center size (d/C), and by intrinsic biological variability. As growth continues and the size of the disks decreases, Fibonacci modes augment due to the fronts' Fibonacci adding property and new convergents are imposed to the divergence angle that have average values close to 2/5, then 3/8, 5/13, etc., thus imposing progressively and more precisely a range of divergence angles that converges, on front-based average, towards the golden angle, while never exactly reaching it. For high order modes, this process traps the divergence angle, keeping it close to the golden angle with an amazing precision, but only *on average*. Therefore, the increase in numbers of parastichies is constrained, canalized, by the number of previous ones, via the front and a slow increase of the CZ. This multiscale canalization process is particularly robust as the fronts can produce many values of divergence angles at the microscopic level without modifying the macroscopic patterns (the parastichies). This is a remarkable example of pattern canalization during development.

This space competition occurs locally, in the notches of the fronts, between two or three preexisting primordia. One notch does not interact with the other notches around, and, except in very small parastichy numbers, the largest notch is not in contact with the last grown primordia, since this one filled some recently free notch. In this way, estimating the divergence angle and plastochron is just a description tool, rather than a construction principle. This seems meaningful since, first, at high d/C (low mode numbers), the probability of organ initiation disorder is very low (Refahi et al. 2016) and the divergence angle oscillates robustly around a relatively stable value, and second, even at low d/C, if that parameter does not change for some time, the models show that the arrangements converge towards rather regular states (Golé and Douady 2020). On compressed structures like pine cones, the parastichies allow to draw a putative generative spiral, and propose an ordering of the primordia. From this a mean divergence and plastochron can be measured. But the positioning is not perfect, there are fluctuations, thus the divergence and plastochron have a meaning only on average (Fig. 7). This is especially true when the position fluctuations are large in elongated stems, such as *Arabidopsis thaliana* inflorescence, which present permutations of the order of appearance of the primordia from a putative regular generative spiral (Besnard et al., 2014), or in large *Asteraceae* inflorescence, where the models (Douady and Couder 1996b) show that the primordia order (and thus divergence) can fluctuate widely, while the overall pattern is regular: the numbers of parastichies are not disturbed, and this allows to define a meaningful averaged divergence.

Epistemological perspective

Phyllotaxis shows how the idealization of a pattern and its mathematical properties can overshadow its development reality. One is irresistibly attracted to think that these properties (convergents, golden angle, Fibonacci) are the deep reason behind the amazing phyllotaxis patterns, overlooking the iterative growth process, and its observable missteps (Jean 2001, Wiss 2012, Besnard 2014, Fierz 2015). It also remarkably illustrates that, while it may be tempting to interpret the development of an organism with striking patterns as the result of natural selection on these patterns, they may just result from developmental constraints, whose dynamics has to be analysed in detail to understand how it can unfold into such surprising motifs. Here the Natural selection is not on any number of spirals or divergence angle, but on the choice between Fibonacci spirals and quasi-symmetry. Before invoking Natural selection to explain a shape, this suggests that one has first to consider the few possibilities left downstream of developmental canalization.

Acknowledgments

We thank Rob Dorit, for useful discussions about developmental canalization, Teva Vernoux and Jan Traas for a long-standing and fruitful collaboration on molecular patterning at the SAM and members of the Reproduction and Development of Plants Lab (RDP) for their encouragement to transform a series of talks on phyllotaxis into a primer paper. We would like to address special thanks to the editor, Alex Eve, for his tremendous help in editing this manuscript, and to the referees for their helpful suggestions and remarks to make this text accessible to a wide audience.

References

Adler, I. (1974), A model of contact pressure in phyllotaxis', *Journal of Theoretical Biology* **45**, 1–79.

Adler, I., Barabé, D. and Jean, R. V. (1997). A history of the study of phyllotaxis. *Ann. Bot.* 80, 231–244.

Alberch, P. (1982), Developmental Constraints in Evolutionary Processes, *in* Evolution and Development, Springer, Berlin, Heidelberg, pp. 313–332.

Alberch, P. (1991), From genes to phenotype: dynamical systems and evolvability, *Genetica* **84**(1), 5–11.

Atela, P., Golé, C. and Hotton, S. (2003), A Dynamical System for Plant Pattern Formation: A Rigorous Analysis, *Journal of Nonlinear Science* **12**(6), 641–676.

Atela, P. (2011), The Geometric and Dynamic Essence of Phyllotaxis, *Mathematical Modelling of Natural Phenomena* **6**(2), 173–186.

Atela, P. and Golé, C. (2007), Rhombic tilings and primordia fronts of phyllotaxis (preprint). http://arxiv.org/abs/1701.01361.

Barbier de Reuille, P., Bohn-Courseau, I., Ljung, K., Morin, H., Carraro, N., Godin, C. and Traas, J. (2006), Computer simulations reveal properties of the cell-cell signaling network at the shoot apex in

Arabidopsis. *Proceedings of the National Academy of Sciences* **103**(5), 1627– 1632.

Battjes, J., Vischer, N. and Bachmann, K. (1993), Capitulum Phyllotaxis and Numerical Canalization in Microseris-Pygmaea (Asteraceae, Lactuceae), *American journal of botany* **80**(4), 419–428.

Besnard, F., Refahi, Y., Morin, V., Marteaux, B., Brunoud, G., Chambrier, P., Rozier, F., Mirabet, V., Legrand, J., Lainé, S., Thévenon, E., Farcot, E., Cellier, C., Das, P., Bishopp, A., Dumas, R., Parcy, F., Helariutta, Y., Boudaoud, A., Godin, C., Traas, J., Guédon, Y. and Vernoux, T. (2014), Cytokinin signalling inhibitory fields provide robustness to phyllotaxis, *Nature* **505**(7483), 417–421.

Bhatia, N. and Heisler, M. G. (2018). Self-organizing periodicity in development: organ positioning in plants. *Development* **145**, dev149336–11.

Braun, A. (1831), 'Vergleichende Untersuchung über die Ordung der Schupper an den Tannenzapfen, als Einleitung zur Untersuchung der Blattstellung u¨berhaupt', *Nova Acta Physico-Medica* **XV**, 191–403.

Bravais, L. and Bravais, A. (1837), 'Essai sur la disposition des feuilles curvis´eri´ees', Ann. Sci. Nat. **7**, 42–110.

Debat, V. and Le Rouzic, A. (2019), Canalization, a central concept in biology, *Seminars in Cell and Developmental Biology* **88**, 1–3.

Douady, S. (1998). The selection of phyllotactic patterns. In *Symmetry in Plants*, pp. 335–358. WORLD SCIENTIFIC.

Douady, S. and Couder, Y. (1992), 'Phyllotaxis as a physical self-organized growth process.', Physical review letters **68**(13), 2098–2101.

Douady, S. and Couder, Y. (1996*a*), Phyllotaxis as a dynamical self organizing process. Part I: The spiral modes resulting from time-periodic Iterations, *Journal of Theoretical Biology* **178**, 255–274.

Douady, S. and Couder, Y. (1996b). Phyllotaxis as a dynamical self organizing process. Part II: The spontaneous formation of a periodicity and the coexistence of spiral and whorled patterns. *Journal of Theoretical Biology.* **178**, 275–294.

Douady, S. and Couder, Y. (1996*c*), Phyllotaxis as a dynamical self organizing process. Part III: The simulation of the transient regimes of ontogeny, *Journal of Theoretical Biology* **178**(3), 295–312.

Douady, S. and Golé, C. (2016), Fibonacci or quasi-symmetric phyllotaxis. Part II: botanical observations, *Acta societatis botanicorum Poloniae* **85**(4)

Fierz, V. (2015), Aberrant phyllotactic patterns in cones of some conifers: a quantitative study, *Acta Societatis Botanicorum Poloniae* **84**(2).

Fowler, D. R., Hanan, J. and Prusinkiewicz, P. (1989). Modelling spiral phyllotaxis. *Computers and Graphics* **13**, 291–296.

Galvan-Ampudia, C. S., Chaumeret, A. M., Godin, C. and Vernoux, T. (2016), Phyllotaxis: from patterns of organogenesis at the meristem to shoot architecture, *Wiley Interdisciplinary Reviews: Developmental Biology* **5**(4), 460–473.

Galván-Ampudia, C. S., Cerutti, G., Legrand, J., Brunoud, G., Martin-Arevalillo, R., Azais, R., Bayle, V., Moussu, S., Wenzl, C., Jaillais, Y.,Lohmann, J, Godin, C. , Vernou, T. (2020). Temporal integration of auxin information for the regulation of patterning. *eLife* **9**, 105–6

Golé, C. (2020). Archimedean spirals, interactive Geogebra program, https://www.geogebra.org/m/q5ysr7bv#material/feycx5yb

Golé, C. and Douady, S. (2020), Convergence of a disk stacking process on the cylinder. *Physica. D* **403 (**132278)

Golé, C., Dumais, J. and Douady, S. (2016), Fibonacci or quasi-symmetric phyllotaxis. Part I: why?, *Acta societatis botanicorum Poloniae* **85**(4):3533.

Golé, C., Godin, C. and Douady, S. (2020). Cylinder and Spiral lattices, Interactive Geogebra program**,** https://www.geogebra.org/m/atpsecjr

Hirmer, M. (1931). Zur Kenntnis der Schraubenstellungen im Pflanzenreich. *Planta* **14**, 132–206**.**

Hofmeister, W. (1868), Allgemeine morphologie der gewashe, *in* Handbuch der Physiologischen Botanik, Engelmann, pp. 405–664.

Hotton, S., Johnson, V., Wilbarger, J., Zwieniecki, K., Atela, P., Golé, C. and Dumais, J. (2006), The possible and the actual in phyllotaxis: Bridging the gap between empirical observations and iterative models, *Journal of Plant Growth Regulation* 25(4), 313–323.

Jean, R. V. (1986). A basic theorem on and a fundamental approach to pattern formation on plants. *Mathematical Biosciences* **79**, 127–154.

Jean, R. V. and Barabé D. (2001). Application of Two Mathematical Models to the Araceae, a Family of Plants with Enigmatic Phyllotaxis. Annals of Botany **88**: 173-186.

Jönsson, H., Heisler, M. G., Shapiro, B. E., Meyerowitz, E. M. and Mjolsness, E. (2006). An auxin-driven polarized transport model for phyllotaxis**.** *PNAS* 103, 1633–1638.

Karpenkov, O. (2013), Geometry of Continued Fractions, Vol. 26 of Algorithms and Computation in Mathematics, Springer-Verlag.

Kirchoff, B. K. (1984). On the relationship between phyllotaxy and vasculature: a synthesis. *Botanical Journal of the Linnean Society* **89**, 37–51.

Koch AJ, Bernasconi G, Rothen F. (1998). Phyllotaxis as a geometrical and dynamical system In: Jean RV, Barabé D. editors. Symmetry in Plants Singapore: World Scientific, 459–48

Kuhlemeier, C. (2007). Phyllotaxis. *Trends Plant Sci* **12**, 143–150.

Kunz, M. (1995) Some analytical results about two physical models of phyllotaxis. Comm. Math. Phys. 169 (2), 261--295.

Livio, M. (2008), The Golden Ratio, The Story of PHI, the World's Most Astonishing Number, Broadway Books.

Ma, Y., Miotk, A., Šutiković, Z., Ermakova, O., Wenzl, C., Medzihradszky, A., Gaillochet, C., Forner, J., Utan, G., Brackmann, K., et al. (2019). WUSCHEL acts as an auxin response rheostat to maintain apical stem cells in Arabidopsis. *Nat Commun* 1–11.

Maynard Smith, J., Burian, R., Kauffman, S., Alberch, P., Campbell, J., Goodwin, B., Lande, R., Raup, D. and Wolpert, L. (1985), Developmental Constraints and Evolution: A Perspective from the Mountain Lake Conference on Development and Evolution, *The Quarterly Review of Biology* 60(3), 265–287.

Mitchison, G. J. (1977), Phyllotaxis and the fibonacci series. *Science* 196(4287), 270–275.

Pennybacker, M., Shipman, P. and Newell, A. (2015), Phyllotaxis: Some progress, but a story far from over, *Physica D: Nonlinear Phenomena* 306, 48–81.

Plantefol, L. (1948), La théorie des hélices foliaires multiples, Masson.

Prusinkiewicz, P. and Lindenmayer, A. (1990), The algorithmic beauty of plants, Springer.

Refahi, Y., Brunoud, G., Farcot, E., Jean-Marie, A., Pulkkinen, M., Vernoux, T. and Godin, C. (2016), A stochastic multicellular model identifies biological watermarks from disorders in self-organized patterns of phyllotaxis. *eLife* **5**, 231.

Reinhardt, D., Pesce, E., Stieger, P., Mandel, T., Baltensperger, K., Bennett, M., Traas, J., Friml, J. and Kuhlemeier, C. (2003),'Regulation of phyllotaxis by polar auxin transport, *Nature* **426**(6964), 255–260.

Richards, F. J. (1951), Phyllotaxis: Its Quantitative Expression and Relation to Growth in the Apex, *Philos Trans R Soc Lond B Biol Sci.* **235**(629), 509–564.

Schimper, K. F. (1835), Beschreibung des symphytum zeyheri und seiner zwei deutschen verwandten der s. bulbosum schimper und s. tuberosum jacq. *Geigers Magazin für Pharmacie* 29, 192.

Schwendener, S. (1878), Mechanische Theorie der Blattstellungen, W. Engelmann, Leipzig.

Smith, R. S., Guyomarc'h, S., Mandel, T., Reinhardt, D., Kuhlemeier, C. and Prusinkiewicz, P. (2006). A plausible model of phyllotaxis. *PNAS* **103**, 1301–1306.

Smith, R. S. and Prusinkiewicz, P. (2006), Inhibition fields for phyllotactic pattern formation: a simulation study, *Canadian Journal of Botany* **84**(11), 1635–1649.

Snow, M. and Snow, R. (1952), Minimum areas and leaf determinatio', *Proceedings of the Royal Society of London B: Biological Sciences* 139(897), 545–566.

Strauss, S., Lempe, J., Prusinkiewicz, P., Tsiantis, M. and Smith, R. S. (2019). Phyllotaxis: is the golden angle optimal for light capture? *New Phyotologist* **45,** 1-12**.**

Swinton, J., Ochu, E. and Consortium, M. T. S. (2016). Novel fibonacci and non-fibonacci structure in the sunflower: results of a citizen science experiment, *Royal Society open science* 3(5), 160091.

Traas, J. (2013). Phyllotaxis. *Development* **140**, 249–253.

van Iterson, G. (1907), Mathematische und microscopisch-anatamische studien uber blattstellungen, nebst betraschungen uber der schalenbau der miliolinen gustav-fischer-verlag, *G. Fischer: Jena* .

Veen, A. (1973), A computer model for phyllotaxis. a network of automata [Master thesis]. Philadelphia, PA: Computer and Information Sciences Graduate School of Arts and Sciences, University of Pennsylvania

Vernoux, T., Brunoud, G., Farcot, E., Morin, V., Van den Daele, H., Legrand, J., Oliva, M., Das, P., Larrieu, A., Wells, D., et al. (2011). The auxin signalling network translates dynamic input into robust patterning at the shoot apex. *Mol. Syst. Biol.* **7**, 508–15.

Wagner, A. (2005). *Robustness and Evolvability in Living Systems*. Princeton University Press.

Wiss, D. and Zagórska-Marek, B. (2012). Geometric parameters of the apical meristem and the quality of phyllotactic patterns in Magnolia flowers. *Acta Societatis Botanicorum Poloniae* **81**, 203–216.

Yadav, R. K., Perales, M., Gruel, J., Ohno, C., Heisler, M., Girke, T., Jönsson, H. and Reddy, G. V. (2013). Plant stem cell maintenance involves direct transcriptional repression of differentiation program. *Mol. Syst. Biol.* **9**, 654.

Zagórska-Marek, B. (1985). Phyllotactic patterns and transitions in Abies balsamea. *Canadian Journal of Botany* **63**, 1844–1854.

Zagórska-Marek, B. (1994). Phyllotaxic diversity in Magnolia flowers. *Acta Societatis Botanicorum Poloniae,* **2***,* 117–137.

Zagórska-Marek, B. and Szpak, M. (2016). The significance of γ-and λ-dislocations in transient states of phyllotaxis: how to get more from less – sometimes! *Acta Societatis Botanicorum Poloniae* **85**, 1–16

Figure legends:

Fig. 1. **Phyllotaxis patterns in a nutshell.** (A) Examples of spiral phyllotaxis (1 organ per node) on different plant parts. (B) Whorled phyllotaxis (more than one organ per node). (C) Individual spirals making up a spiral pattern are called parastichies. (D) Parastichies come generally in two (or three) families of spirals: clockwise and counterclockwise. The numbers of parastichies in these 2 families are most of the time consecutive numbers in the Fibonacci sequence (E) Sometimes, a third more vertical parastichy family appears, called orthostichy (red line) (Box 2) like on the fruit of *Encephalortos horridus*. (F) The SAM: the organ factory (here the inflorescence meristem of *Arabidopsis thaliana*, photo courtesy of Jan Traas). Organs are generated sequentially at precise positions on the flank of the meristem separated by a relatively constant divergence angle. (G) In general, the divergence angle remains unchanged after internode elongation (here, inflorescence of *Arabidopsis thaliana*). (H) The spiral made by the imaginary curve joining the consecutive organs is called the generative spiral. If one considers a pair of leaves with similar orientation on the stem (blue), it is easy to estimate the average divergence angle separating these two leaves: here, mean divergence angle=#turns/#organs = 5/13 = 0.385 turn =138.5°. (I) If we (virtually) contract this structure, the leaves that are in the same direction get visually close to each other. (J) In many cases they do not exactly overlay and present actually a small angular deviation. This deviation spreads along the contracted structure and generates visual spirals (the parastichies and orthostichies).

Fig. 2. **Testing the relation between divergence angle and emerging phyllotaxis motifs using a simple kinematic model.** (A) Simple kinematic model: Organs (orange dots) are initiated at the periphery of the central zone (green disk). Primordia are initiated with a constant period T during the simulation and move radially away from the center at a constant velocity V=1.0 arbitrary length unit / arbitrary time unit. The value of the radius is fixed to 1 arbitrary length unit. (B) Intuition: the arms look straight for rational values and their number depends on the divergence angle. (C) For α=1/5 and α=2/5, the arms are numbered (in orange) and the first initiated organ (at t = 0) is at the outermost end of arm 1 (green arrows labeled with 1). For α=1/5, the second initiated organ is at the outermost end of arm 2 (green arrows labeled with 2), etc. However, for α=2/5, the second initiated organ appears at the outermost end of arm 3, separated from arm 1 by an angle of 2/5, and the third initiated organ appears at the outermost end of arm 5, etc. (D) Slowly changing the divergence from an initial rational value (here 2/5) shows that arms can bend and even change in number. (E) Decreasing the value of the plastochron while keeping the divergence angle constant, here α=41/100, also induces bending of spiral arms. After some point, the spirals merge and a new set of arms appears – here 5 original bending arms (left) are progressively replaced by 17, 22, 39 and 100 straight arms (right, close-up).

Fig. 3. **Divergence angle convergents**. (A) For each pattern (here for G=0.1, α=41/100), one can observe the spiraling arms in two families of parastichies (only one if the arms are straight), turning in opposite directions, as in plants, and whose number are often consecutive denominators in the list of convergents of the divergence angle, here $\frac{1}{2}, \frac{2}{5}, \frac{7}{17}, \frac{9}{22}, \frac{16}{39}, \frac{41}{100}$ are the convergents of $\frac{41}{100}$. The number of spirals in these two families

define the mode. At T = 0.1 for example, the mode is (5,17). When T decreases, the spiral motif passes successively through modes (1,2), (2,5), (5,17), (22,17), (22,39) until we reach the 100 straight arms configuration, where the other 39 spirals are no longer visible. (B) When the divergence angle is the golden angle, for decreasing growth index G, the spiral motif passes through modes (1,2),(2,3),(3,5),(5,8),(8,13),… that are consecutive denominators in the series of convergents of the golden angle. These pairs of numbers are consecutive numbers of the Fibonacci sequence. (C) Drastic change of spiral patterns in the neighborhood of the golden angle (the growth index is fixed to G = 0.1).

Fig. 4. **Spiral and cylinder lattices.** (A) Top (centric) view of a spruce meristem (micrograph courtesy of Rolf Rutishauser). The primordia shown here were to form pine needles. They are numbered by increasing age. There are 8 green contact parastichies and 13 red ones. The divergence angle is not far from the golden angle. Dashed lines indicate the front for this plant. (B) Logarithmic spiral lattice structure with (8, 13) mode mimicking the spruce in (A) The virtual primordia are expanding away from the CZ at a speed proportional to their distance from the center. (C) Cylindrical view of a digitally unrolled pineapple. The vertical white lines represent the same line on the pineapple, and points P and P' are also identical there. Dashed segments indicate the front when P was the newest primordium. (D) A cylinder (rhombic) lattice corresponding to the spiral lattice in (B) in a specific mathematical sense. Its parastichies are parallel lines on the unrolled cylinder. Note that there is no contact between organs 0 and 1, or 1 and 2 etc. Instead, 0 is in contact with its older contact neighbors 8 and 13. These also give the number of parastichies. The black rhombus shows that parastichies draw rhombii. (E) van Iterson diagram (in black) in the (α, G) plane - where α is the angular displacement (divergence angle) and G the vertical displacement between a point and the next one up in a cylindrical lattice. Regions of constant mode (i, j) are colored. Points labelled (a)-(d) correspond to the lattices shown with same labels, and e corresponds to Fig. D. Lattice **(**a**)** is not rhombic: the parastichy through 0, 2 and 4 etc. is not a contact parastichy. The lattices (b)-(e) on the other hand are all rhombic: their parastichies join disks in contact and they draw a repeating pattern of rhombi. Accordingly, they all belong to the upside-down tree-like van Iterson diagram (in black), formed by the vertical segment in region (1, 1) (the trunk) and otherwise arcs of circle (the branches).

Fig. 5. **Fronts as Fibonacci machines.** (A-A″) Fibonacci transition from 5, 3 to 5, 8: the starting front in (A) has 5 up, 3 down segments. The up segments are roughly parallel, as are the down segments. Disks are stacked with decreasing size. At first the transitions are all quadrilateral, without changes in parastichy numbers. (see B′). But as the disks become smaller, the notches of the front open up, forcing triangle transitions (A′). Since disks seek the lowest available space, these occur on the flatter segments (the green, up segments here, as there are more of them than the red). Each triangle adds an extra (red) down segment, for a total of 5 new down segments which, added to the 3 old ones, gives 8 of them. On the other hand, there are no added up (green) segments, but the existing ones have become more slanted, with roughly equal angles. The regularity is preserved, and this new Fibonacci front sets the stage for the next round. (B) A Triangle transition occurs because the angle of the notch 10-7-8 is too wide to form a rhombus: a disk tangent to 10 and 8 would necessarily intersect 7. The new disk, 12 here, is tangent to 7 and 8, the side of the notch that is flattest. The insert shows that other choices either overlap or are higher. Segment 12-8 is a net addition of a red segment, increasing the front down-parastichy number by one. (B′) a quadrilateral transition keeps the parastichy numbers unchanged. (B″) A pentagon

transition decreases a parastichy number by 1. This time, the angle between the segments 10-13 and 7-12 is too small to allow a rhombus.

Fig. 6. **Fibonacci transitions *in vivo* and *in silico*.** (A) Unrolled ornamental cabbage with removed leaves. The pattern of line segments joining adjacent leaf scars, shows a sequence of Fibonacci transitions from (1, 1) to (5, 8) via a succession of clusters of triangle transitions that alternate sides. (B) Although no attempt was made to exactly match the cabbage pattern, this computer simulation, where the diameter *d* of the disks decreases linearly with their height, shows the same alternating pattern of triangle transitions between (1, 1) and (5, 8). (B′) Graph of front parastichy numbers as function of the number of iterations, from the simulation in (B), showing the red and green parastichy numbers monotonically increase one by one to the sum of the previous two. This is a signature of regular Fibonacci transitions, easily detectable in computer simulations. (C) Filled-in inflorescence meristem of an artichoke (SEM courtesy J. Dumais). (C') Graph obtained by drawing all the successive fronts on the artichoke inflorescence in (C). Three concentric fronts are shown, with parastichy numbers (34, 55), (34, 21) and (13, 21) transitioning via pentagons as fronts move closer to the center.

Fig. 7. **Fronts and angle of divergence.** (A, A′) (3,2) and (8, 5) fronts (blue), and the next disk (dark pink) show the emergence of the golden angle, as their parastichy numbers increase through the Fibonacci sequence. These fronts, extracted from rhombic lattices, have each identical up and identical down segments. (A′′) A slight, random perturbation of the front in A′ (the last down and up segments to the right of the front are slightly different from the others in the front). It results in a change in the order of initiation of primordia: whereas the divergence for the first and second new disk was roughly γ in A′, it is close to γ and 2γ in this case. (B, C) Angle of divergence at each iteration of the simulation of Figure 6B. While at first the divergence seems to converge towards the golden angle α, it then starts oscillating widely. However, the values it hits are all close to multiples of α. This is explained by permutations of the vertical order of the disks, as in A′′. (D) The permutations seen in (B) are averaged out when taking the mean of the divergence angle over a front: in the right coordinate frame, the solid curves in this graph espouse closely the Fibonacci branch of the van Iterson diagram of Fig. 4E. The dashed lines correspond to triangle transition irregularity (the triangle transitions cannot all happen at the same level and at the same time). (E) Visualization, in the (d, α) coordinates. of the points in the same simulation as in (B). Points outside the range shown were omitted. In blue, the van Iterson diagram, as represented in these coordinates. (E') Same data as in (E), but averaged over one rolling front. Note the striking fit to the diagram.

Fig. 8. **Free space for next primordia (in model and observed auxin maps).** (A) a (3,2) front of disks, with an inhibitory field diffusing from them to indicate the free space around them. Three holes are visible at different heights. The position of the next disk is indicated by a dotted circle, as well as the position of the rim of the central zone by a dashed line. The arrow indicates the minimum where the new disk will be placed (A') Field value at the line corresponding to the rim of the central zone, indicated by the dashed line. The arrow indicates here as well the position of the new disk. (B) Average map of qDII (quantitative negative auxin reporter: auxin is high in dark region, and low in bright regions) after registration of several SAMs imaged with a confocal microscope (adapted from (Galvan-Ampudia et al., 2020)). The young organs deplete auxin at the CZ periphery (dotted circle)

and create altogether a front that prescribes the positions of the new primordium (indicated by an arrow). (B’) corresponding qDII profile unrolled along the CZ periphery. Its minimum (arrow) indicates the position of the next primordia. This curve, obtained from quantitative measurement of auxin on real SAMs (Galvan-Ampudia et al., 2020), strikingly parallels the inhibitory curves (A’) obtained from front diffusion in simple disk stacking models (A).

Phyllotaxis as geometric canalization during plant development

-

SUPPLEMENTARY INFORMATION

Christophe Godin, Christophe Golé, Stéphane Douady

July 19, 2020

These supplementary information sections are intended to provide some definitions and key mathematical details for the interested readers.

1 Definitions of the concept of canalization in biology

There exists a number of uses of the term canalization in both evolutionary and developmental biology. As noted by (Debat and David, 2001), "*the literature [about canalization, phenotypic plasticity and developmental stability] can be confusing because the historical definitions usually referred to do not take into account later conceptual and empirical advances*".

Canalization can be primarily considered as a developmental process. According to B. Hall (2012) for instance, "*Canalization (or developmental buffering) is the process whereby the more invariant characters of an organism are channeled into restricted sets of developmental pathways - the valleys in Waddingtons epigenetic landscape (Waddington, 1942) -*". Originally Waddington (1942; 1953), defined it as "*the ability to produce a consistent phenotype in spite of variable genetic and/or environmental features.*"

Canalization can also be considered as an evolutionary process. This second meaning was already used by Waddington (1961), who introduced the idea that canalization may itself be under genetic control, what is usually termed canalizing selection. This is clearly put by Gibson & Wagner (Gibson and Wagner, 2000): "*for the evolutionary biologist, canalization is genetic buffering that has evolved under natural selection in order to stabilize the phenotype.*"

In this paper, the term canalization refers to developmental canalization (first definition above), and not to canalizing selection. Modern definitions of developmental canalization have been suggested by different authors. Wagner (2005), for example, proposes: "*An organismal feature is canalized if its embryonic development is insensitive to variations in the environment or in the genes*". Such canalization can be due to various types of developmental constraints, reviewed for instance in (Maynard Smith et al., 1985). We suggest here that phyllotaxis is primarily governed by geometric developmental constraints (coming from the physical/chemical interactions between young organs at the tip of growing shoots) that buffer possible noise, be it biological, genetic or environmental.

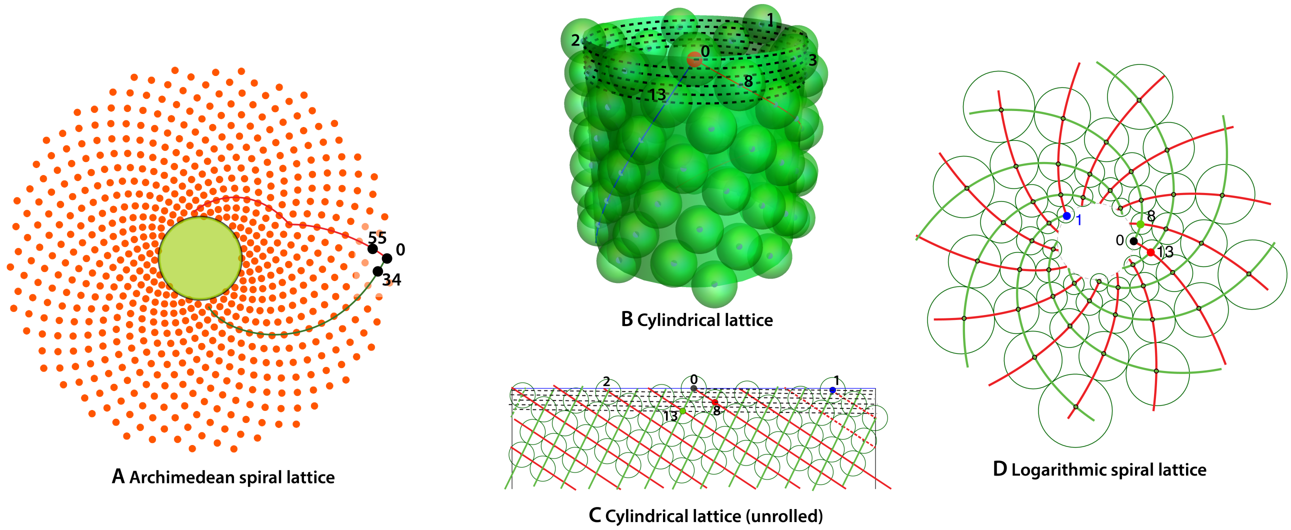

A Archimedean spiral lattice

B Cylindrical lattice

C Cylindrical lattice (unrolled)

D Logarithmic spiral lattice

Figure S1: **Common geometric representation of phyllotaxis patterns**. (A) Centric representation with growth index linear in the plastochron, yielding Archimedean spirals. The parastichy numbers are (55, 34), but the 55-spirals are replaced by 21-spirals near the center. (B) Cylindrical lattice representation (e.g. pineapple), with parastichy numbers (8, 13). Dashed black: the generative helix, along which every lattice point is arranged at regular intervals (here the golden angle). The parastichies (through 8 and 13) are less tightly wound helices. (C) The cylindrical lattice from B, but shown unrolled. The generative spiral and the parastichies are straight lines in this representation, with pieces cut and translated in the central domain represented. (D) The exponential spiral lattice corresponding to the lattice in (C) under the complex exponential map. Note that contacts between primordia are preserved by the mapping, and that primordia are not quite circular.

2 Geometric representations of regular phyllotaxis

Regular patterns produced around the meristem of a plant can be represented in different geometries that are more or less suitable depending on plant species and growth stages. To represent a (regular) plant pattern at the vegetative stage for example, a cylindrical lattice often captures much of plant leaf arrangements around the stem. At the same time, the area immediately around the meristem may show, when seen from above in the centric representation, an exponential growth of the size of the primordia, with a corresponding exponential increase of their distance to the center Fig. S1.

At the inflorescence stage, in some plants (e.g. asteracea) the meristem grows in width and flattens, while in the time frame of their formation at this stage, the flower primordia remain of roughly equal size, filling in the enlarged meristem. As a consequence, their distance to the center decreases *linearly* in time.

Assuming the pattern has a constant divergence angle, *i.e.* it is regular, three common types of patterns of points are used to describe the arrangement of the centers of primordia. In each case the pattern is generated by points on one *generative spiral* or helix. The generative spirals (resp. helices) are of the form:

1. **Archimedean spiral:** $s \to (R(1+sG)\cos 2\pi s\alpha, R(1+sG)\sin 2\pi s\alpha)$
2. **Helix on the cylinder:** $s \to (R\cos 2\pi s\alpha, R\sin 2\pi s\alpha, RsG)$

3. **Straight line on the unrolled cylinder:** $s \to (Rs\alpha \mod 2\pi R, RsG)$
4. **Logarithmic or Bernouilli spiral:** $s \to \left(Re^{sG'} \cos 2\pi s\alpha, Re^{sG'} \sin 2\pi s\alpha\right)$

With R the radius of the central zone, G the growth index (and $G' = 2\pi G$), α (in units of number of turns) the divergence between successive lateral organs.

The points of the lattice are obtained by taking $s = 0, 1, 2, 3, \ldots$ (sometime in reverse order). In all cases the parastichies are the same kind of curve as the generative one, but going through "multiples": if point 8 is the closest point to 0 for instance, then one parastichy passes through points labelled 0, 8, 16, 24 etc... but no other lattice point. This helical parastichy would then have equation $s \to (R \cos 2\pi s\alpha, R \sin 2\pi s\alpha, 8sG)$. Another one goes through 1, 9, 17, 25 etc., with equation $s \to (R \cos 2\pi(s\alpha + 1/8), R \sin 2\pi(s\alpha + 1/8), 8sG)$. and there are 8 distinct parastichies in that family (add multiples of 1/8 in the formula).

In this paper, we used Archimedean spirals in Sections 2 and 3, as they are more compact, with points closer to one another, and thus easier to connect mentally, without having to draw primordia as extended disk-like regions. The reader can explore these patterns with the Archimedean Geogebra app (Golé, 2020)).

The cylindrical and logarithmic spiral lattices are introduced in Section 4, and are used thereafter. The reader can interact with both these patterns in the Spiral & Cylinder lattices Geogebra app (Golé et al., 2020)).

In that second app, as well as figures in this paper, we make use of the fact that there is a natural transformation between the cylindrical and spiral patterns. Indeed, when using the complex representation $z = \alpha + iG$ of (α, G), a natural correspondence between the two models is

$$z \to e^{i2\pi\bar{z}}.$$

Accordingly, in the app, we represented each logarithmic spiral lattice above the unrolled cylindrical lattice it corresponds to and used the (α, G) plane as the parameter plane, in which the user can choose a point, and hence a lattice, interactively. This correspondence explains our use of $G' = 2\pi G$ in the formula for the logarithmic spiral above. We mapped not only the centers of the lattices to the corresponding spiral lattice points, but we also used the exponential map above to transform the parastichies into logarithmic as well as the circles representing the primordia to closed curves that preserve the contacts of the lattice disks.[1]

For a cylindrical lattice (Fig. S1C), the vertical displacement between one lateral organ and the next is RG (G dimensioned by the cylinder radius R). When putting N primordia, the total vertical displacement is thus NRG. Multiplying by the cylinder circumference $C = 2\pi R$ this gives the total cylinder surface used during this process as $S = NRCG = 2\pi NR^2G = (N/2\pi)C^2G$. In the same time, we placed N little discs of diameter d, covering a surface of $N\pi d^2/4$. If they are placed with a density η, $\eta = (N\pi d^2/4)/S$ so we have the total surface of $S = N\pi d^2/4\eta$. Equalling the two expressions gives $G = (\pi^2/2\eta)(d/C)^2$ as mentioned in Box 2.

---

[1] Note that this is an unusual choice: Starting with van Iterson (1907), researchers have mostly considered logarithmic spiral lattices where primordia are modeled by circles and considered a diagram that locates those spiral lattices with two sets of contact parastichies, very similar (but not identical) to the one for rhombic cylindrical lattices (Yamagishi and Sushida, 2017).

3 Convergents: the best rational circular approximations of a real number

The notion of *convergents* of a real number is key to the understanding of the connection between divergence angles and spirals. It relies on the fact that each real number can be increasingly well approximated by a unique sequence of fractional (rational) numbers called *its convergents*. This section explains how the convergents of a real number x are derived and why, with some mathematical details.

Best rational approximations of a real number. Let us consider a real number x (chosen here without loss of generality between 0 and 1 for sake of simplicity), for example 0.43. We want to subdivide the interval [0,1] into q pieces of size $1/q$, and find the number of pieces p of size $1/q$ that best approximates the real number $x = 0.43$ (see Box 2 in main text).

For a given size of piece, $1/q$, all the possible numbers between 0 and 1 that can be made with pieces of size $1/q$ can be enumerated. They are the $q+1$ numbers: $\frac{0}{q},\frac{1}{q},\frac{2}{q},\ldots,\frac{q-1}{q},\frac{q}{q}$ (Fig. S2.A left: pyramid of rationals whose denominator is ≤ 100).

We can compute for each of these fractions $\frac{p}{q}$ the distance to the approximated real x:

$$d\left(x,\frac{p}{q}\right) = \left|x - \frac{p}{q}\right|, \tag{1}$$

If for one of these fractions, $\frac{p}{q}$, this distance is smaller than any other distance with denominator less than or equal to q, $\frac{p}{q}$ is called *the best approximation of x with pieces of size* $1/q$ (see Box 2). If no such fraction is found for pieces of size $1/q$, then the best approximation of x with pieces of size $1/q$, is the last found best approximation of x with pieces of size $1/q'$, $q' < q$.

For example, setting $q = 1$, the fraction 0/1 is a better approximation of 0.43 than fraction 1/1, as 0.43 is closer from 0 than from 1. Fraction 0/1 is thus the best rational approximation of 0.43 with pieces of size 1/1. For $q = 2$, fraction 1/2 is closer to 0.43 than 0/2 and than 2/2. Fraction 1/2 is thus the best approximation of 0.43 with pieces of size 1/2. For $q = 3$, none of the fractions $0/3, 1/3, 2/3, 3/3$ is closer to 0.43 than 1/2. Therefore 1/2 is the best approximation of 0.43 with pieces of size 1/3, and so on. As q increases (and the size of the tile $1/q$ decreases), increasingly better approximations of the real x may be found (fractions circled in green in Fig. S2). The search terminates when all possible sizes of tiles have been checked out, i.e. in our example after having tried $q = 1, 2, 3, \ldots, 100$. The list of found fractions is the set of best rational approximations of x. If x is a rational, this list is finite. If x is an irrational this list is infinite.

Circular distance of a rational to a real number. In plants we are interested not only in comparing divergence angles, but also in how much one gets back close to the origin after q organs have been initiated with a fixed divergence angle. This is why we are interested in a slightly modified definition of the notion of best approximation of an angle.

Consider the star-like motif of Fig. S3, obtained for a divergence angle of $3/7 = 0.4286$ with the toy model desscribed in the main paper. During the simulation, the first initiated organ, referenced as *the origin*, initiated at the rim of the central zone on the right (Fig. S3.A) went all the way to the right. Subsequent organs were initiated consecutively at azimuthal angles $3/7 = 0.4286, 6/7 = 0.8572, 9/7 = 1.2858, \ldots$ from this initial azimuthal direction. After three complete turns accomplished by organs 2 to 7, the 8th organ is initiated in the same azimuthal direction as the origin (indicated by a downward arrow, Fig. S3.A). After 7 organs, the system

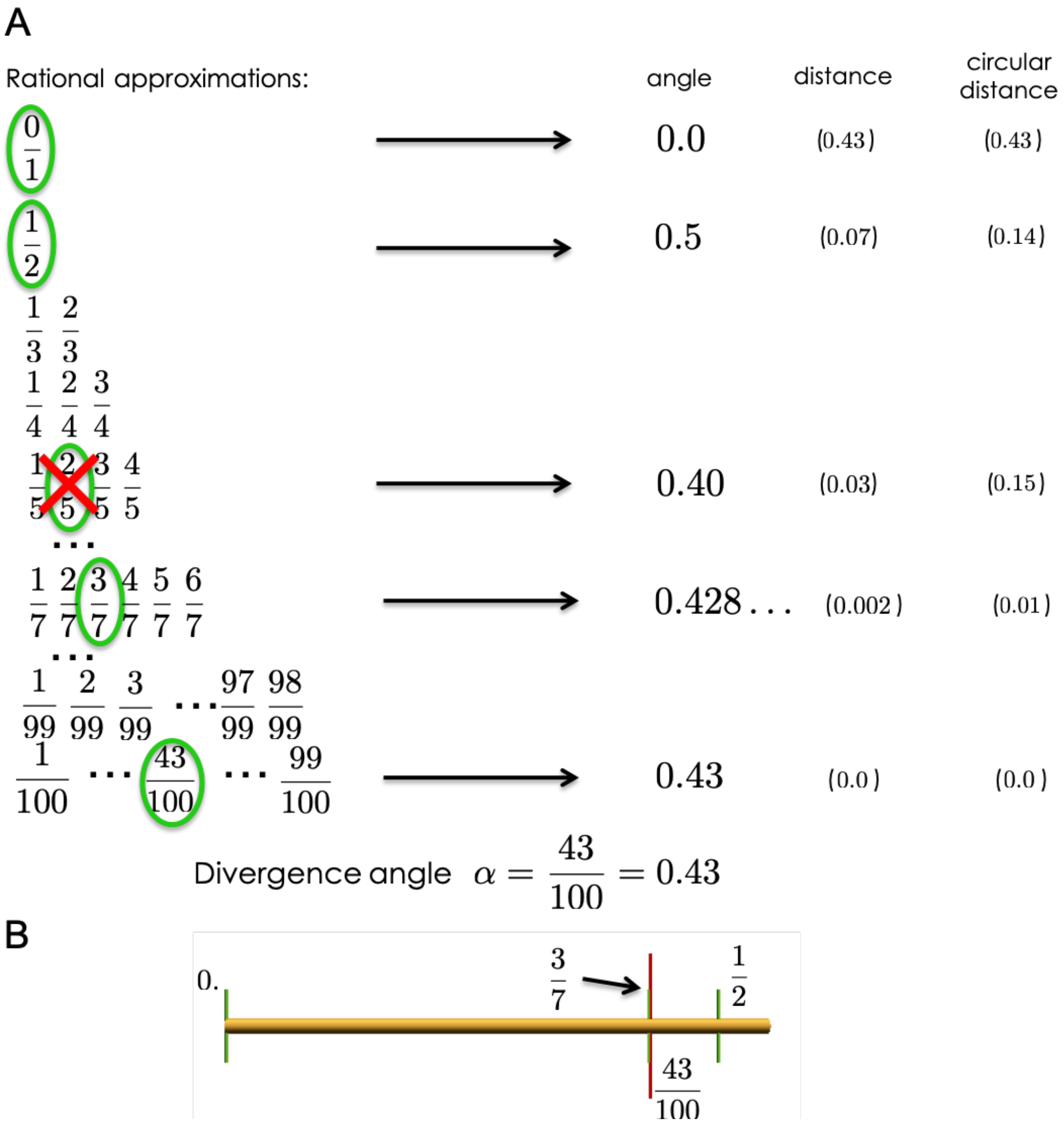

Figure S2: **Construction of the sequence of convergents for 0.43**. (A) Pyramid of all fractions that are less than 1 with denominator less than 100 and ordered by increasing denominators and by increasing numerators in denominators they have equal denominator. Green circles indicates the fractions that are best rational approximations of 0.43. Convergents are a subset of this set. Here, we have to remove 2/5 from the list of best rational approximations to obtain the list of best rational circular approximations of 0.43, i.e. its convergents. The criterion used to select a fraction in the list of convergents is whether it gives a lower circular distance than all preceding fractions with lower or equal denominator (B) Graphical positions of the convergents of fraction 43/100 (note that 3/7 (small green vertical bar) is a very good approximation of 0.43 and appears slightly to the left of 43/100 (large red vertical bar)).

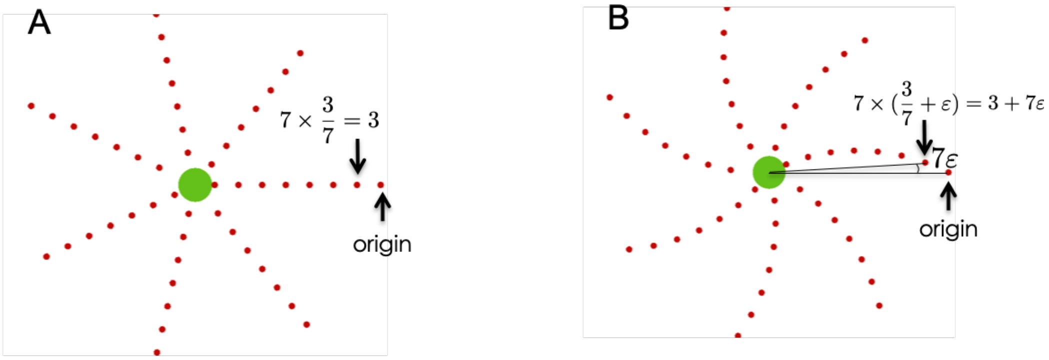

$\alpha = \frac{3}{7} = 0.4286$ $\alpha = 0.43 = \frac{3}{7} + \varepsilon$

Figure S3: **Definition of the circular distance**. A. The circular distance is null for a rational divergence angle p/q after q organs have been generated. B. However, in general, the circular distance is non-null for a divergence angle (rational or not) after q organs have been generated. This non-null circular distance is responsible for the apparition of bending arms (spirals)

with divergence angle 3/7 gets back exactly in the same azimuthal orientation as initially (Fig. S3.A):

$$7 \times \frac{3}{7} = 3,$$

i.e. after 3 complete turns. The fact that the organs are initiated in *exactly* the same azimuthal direction every 7th initiation generates the seven straight arms of the figure.

Let us now slightly increase the value of the divergence angle to 0.43 (Fig. S3.B). At the end of the simulation, the origin organ, which has just been displaced radially with unit speed as before, has reached exactly the same position as in the previous simulation. However, now subsequent organs are initiated at successive angles $0.43, 0.86, 1.29, \ldots$. At the 7th initiation after the initial organ (indicated as origin on Fig.3.B), the angle is now 3.01, a bit more than exactly 3 turns (organ indicated by a downward arrow in Fig. S3.B). Indeed, if we consider that $0.43 = 3/7 + \epsilon$, where ϵ is a small value (here 0.0014), then at the 7th initiation, the angle is:

$$7 \times \left(\frac{3}{7} + \epsilon\right) = 3 + 7\epsilon.$$

The discrepancy with the case of $\alpha = 3/7$ showing straight arms is thus $7\epsilon = 0.0098$. We say that $\frac{3}{7}$ is a *circular approximation* of 0.43 with *circular distance of* 0.0098. 3 is called *number of turns before return*. In the simulation, the same circular distance is systematically observed between organs whose initiations are separated by 7 plastochrons. It is responsible for the bending of arms into spirals.

Formally, for a rational $\frac{p}{q}$, we define the circular distance of $\frac{p}{q}$ to x as:

$$d_c\left(x, \frac{p}{q}\right) = q.\left|x - \frac{p}{q}\right| = |qx - p|.$$

This distance evaluates how close $q.x$ is to integer p. In the context of angles, it actually evaluates how close the organ generated at the qth plastochron is to an integer p number of turns, *i.e.* returns to the initial orientation, assuming organs have been generated with a constant divergence angle x.

Convergents: best rational circular approximations of a real. Given a real x, if a given fraction $\frac{p}{q}$ has a circular distance to x that is better than the circular distance of any other fraction with denominator less than or equal to q, the fraction $\frac{p}{q}$ is called the best rational circular approximation of x with pieces of size q, or a simply *convergent* of x.

The set of best rational circular approximations of x defines the convergents of x. However, one must be careful as not all best rational approximation of x is necessarily a convergent of x. To see this, let us get back to our example (Fig. S2.A), starting with $q = 1$, fraction 0/1 has a circular distance $x = 0.43$ smaller than that of 1/1 and than that of any other q less than 1. 0/1 is thus a convergent of 0.43. For $q = 2$, 1/2 is a better approximation of 0.43 (circular distance = 0.14) than convergent 0/1 (circular distance = 0.43). Then, proceeding with the exploration of fractions with increasing q's, we find for $q = 5$ a fraction 2/5 which is closer to 0.43 than 1/2 (its distance to 0.43 is 0.03), meaning that 2/5 belongs to the set of best rational approximation of 0.43. However, 2/5 has a higher circular distance to 0.43 than 1/2, meaning that after $5 \times 0.43 = 2.15$ turns, we get no closer to the origin than $2 \times 0.43 = 0.86$. 2/5 is therefore not a convergent of 0.43. We need to wait for $q = 7$ to find a fraction $3/7 = 0.428\ldots$, whose circular distance is $7 \times 0.43 - 3 = 0.01$ is better than that of 1/2.

In this way, by looking at the increasing values of q, we find a list of fractions that have increasingly better circular distance to the real number x. This list defines the list of convergents of x, i.e. the list of best rational circular approximations of x. For example, $x = 0.43$ can be increasingly better approximated (in a circular sense) by the sequence of rational numbers:

$$[\frac{0}{1}, \frac{1}{2}, \frac{3}{7}, \frac{43}{100}].$$

They are called the convergents of 0.43.

4 Computation of convergents using continued fractions

The previous section explained what are the convergents of a real number by exploring the list of all fractions with increasing denominators. Fortunately, there exist algorithms to compute the list of convergents of a real number without the need of exploring the set of all fractions. This method is based on the representation of a real number as a *continued fraction* (see e.g. (Karpenkov, 2013)).

Continued fraction associated with a real. Let us consider a positive real x, and denote a_0 the integer part of x. Then if r_0 denotes the decimal part of x, $0 \leq r_0 < 1$, one can write:

$$x = a_0 + r_0.$$

if $r_0 \neq 0$, then $\frac{1}{r_0} > 1$. If a_1 denotes the integer part of $\frac{1}{r_0}$ and r_1 its decimal part, we have:

$$\frac{1}{r_0} = a_1 + r_1.$$

Leading to the following expression of x:

$$x = a_0 + \frac{1}{a_1 + r_1}$$

The decomposition can be continued as long as the decimal part, which is by definition < 1, is non zero. Denoting a_2 the integer part and r_2 the remainder of $\frac{1}{r_1}$, we can write:

$$\frac{1}{r_1} = a_2 + r_2.$$

This series of decompositions, derived from Euclid's algorithm, leads to the following general expression of x:

$$x = a_0 + \cfrac{1}{a_1 + \cfrac{1}{a_2 + \cfrac{1}{a_3 + \cdots}}}.$$

This Russian doll of a fraction, usually denoted $[a_0; a_1, a_2, ...]$ is called the *continued fraction expansion of* x.

For example, the rational $\frac{41}{100}$ can be decomposed using the Euclidean algorithm successively as:

$$\begin{aligned}
\frac{41}{100} &= 0 + \frac{41}{100}, \\
\frac{1}{41/100} &= \frac{100}{41} = 2 + \frac{18}{41} \Rightarrow \frac{41}{100} = \frac{1}{2 + \frac{18}{41}} \\
\frac{1}{18/41} &= \frac{41}{18} = 2 + \frac{5}{18} \Rightarrow \frac{41}{100} = \cfrac{1}{2 + \cfrac{1}{2 + \cfrac{5}{18}}} \\
\frac{1}{5/18} &= \frac{18}{5} = 3 + \frac{3}{5} \Rightarrow \ldots \\
\frac{1}{3/5} &= \frac{5}{3} = 1 + \frac{2}{3} \\
\frac{1}{2/3} &= \frac{3}{2} = 1 + \frac{1}{2} \\
\frac{1}{1/2} &= \frac{2}{1} = 2 + 0
\end{aligned} \tag{2}$$

leading to the continued fraction expansion of $\frac{41}{100}$:

$$\frac{41}{100} = \cfrac{1}{2 + \cfrac{1}{2 + \cfrac{1}{3 + \cfrac{1}{1 + \cfrac{1}{1 + \cfrac{1}{2}}}}}}$$

Or, using the short hand notation:

$$\frac{41}{100} = [0; 2, 2, 3, 1, 1, 2].$$

Contrary to the decimal expansion, one can show that the continued fraction expansion of a rational is always finite. For instance: $\frac{2}{3} = [0; 1, 2]$. On the other hand the continued fraction of an irrational must be infinite. For instance

$$\pi = [3; 7, 15, 1, 292, 1, 1, 1, 2, \ldots]$$

continues forever. The computation of the continued fraction expansion of an irrational, for example π, assumes that we know its decimal expansion to some length, but otherwise proceeds very much as for a fraction:

$$\begin{aligned} \pi &= 3.1415\ldots = 3 + 0.1415\ldots \\ \frac{1}{0.1415\ldots} &= 7.06714\ldots = 7 + .06714\ldots \\ &etc. \end{aligned} \tag{3}$$

Convergents of a real from continued fractions. When truncated by removing all the trailing terms after a certain rank k, the continued fraction expansion of a real number x defines a continued fraction that is the expansion of a rational number. This rational x_k is an approximation of x, with a precision that increases with the rank of the truncation. We will see that in fact this approximation is as good as it could be. These rational values are actually the *convergents* of x.

Formally, if $x = [a_0; a_1, a_2, ...]$ is a continued fraction expansion of x, then the truncated fraction $x_k = [a_0; a_1, a_2, ..., a_k]$ is a continued fraction called the kth *convergent* of x. Explicitly:

$$x_k = a_0 + \cfrac{1}{a_1 + \cfrac{1}{\ddots + \cfrac{1}{a_k}}}.$$

Since x_k is a rational, it can be written as $x_k = \frac{h_k}{p_k}$. It can be shown that the sequence of the denominators p_k increases with k, and that the sequence $\{x_0, x_1, x_2, ..., x_k, ...\}$ of convergents of x are rationals that get closer and closer to x as k increases. Consecutive convergents oscillate around x and are successively greater and lower than x.

The degree of approximation can be estimated quantitatively. Let us denote $x_k = \frac{h_k}{p_k}$, the kth convergent of x, then it can be shown that:

$$\frac{1}{p_k(p_k + p_{k+1})} \leq |x - x_k| \leq \frac{1}{p_k . p_{k+1}}$$

For example, the convergents of $x = 0.43$ are $(0, \frac{1}{2}, \frac{3}{7}, \frac{43}{100})$. Convergent $\frac{3}{7}$ approximates 0.43 with a precision bounded by:

$$\frac{1}{749} = 1.3\,10^{-3} \leq |0.43 - \frac{3}{7}| \leq \frac{1}{700} = 1.4\,10^{-3}$$

Interestingly, this can be used to compute the uncertainty on the value of thee estimated average divergence angle in plants. Assume for instance that a plant presents organs arranged in 13 clockwise and 21 anticlockwise spirals, then we can deduce that these organs correspond to an average divergence angle comprised between angles 21/13 and 34/21 and that the uncertainty on this angle is lower than $1/(13 * 21)$, i.e. $3.7\,10^{-3} = 1.3°$.

The Golden number ϕ has a remarkable continued fraction expansion. From eq. 7 in Box 1, we extract the classical identity:

$$\phi = 1 + \frac{1}{\phi},$$

which can be expanded recursively in the infinite continued fraction expression:

$$\phi = 1 + \cfrac{1}{1 + \cfrac{1}{1 + \cfrac{1}{1 + \cfrac{1}{...}}}}.$$

This makes it possible to compute the convergents of ϕ as the successive truncated fractions obtained from its continued fraction expansion:

$$\frac{1}{1}, \frac{2}{1}, \frac{3}{2}, \frac{5}{3}, \frac{8}{5}, \frac{13}{8}, \frac{21}{13}, \frac{34}{21}, \frac{55}{34}, \frac{89}{55}, \frac{144}{89}, \ldots. \tag{4}$$

Let's see now how the Bravais probably derived the value of the Golden Angle as the only number who has convergents the sequence:

$$\frac{1}{2}, \frac{2}{5}, \frac{3}{8}, \frac{5}{13}, \ldots$$

(quotients of Fibonacci numbers that are two appart in the sequence). As we said in Section 3 of the main text, they must have first computed the continued fractions of a few elements of this sequence and found (using the algorithm we have used for $\frac{41}{100}$ above, which they perform on an example in a footnote):

$$[0; 2], [0; 2, 1], [0; 2, 1, 1], [0; 2, 1, 1, 1], [0; 2, 1, 1, 1, 1] \ldots$$

From which they deduced (or proved?) that these quotients were all convergents of the same infinite continued fraction:

$$\gamma = [0; 2, 1, 1, \ldots]$$

(γ is our notation). The algebra they might have used to compute $\gamma = \frac{1-\sqrt{5}}{2}$ probably looked like this: Since

$$\gamma = \cfrac{1}{2 + \cfrac{1}{1 + \cfrac{1}{1 + \dots}}},$$

we have:

$$\frac{1}{\gamma} = 2 + \cfrac{1}{1 + \cfrac{1}{1 + \cfrac{1}{1 + \dots}}}$$

Call this last term $2 + X$ for short. Then $X = \frac{1}{\gamma} - 2$ and :

$$\frac{1}{X} = 1 + \cfrac{1}{1 + \cfrac{1}{1 + \cfrac{1}{1 + \dots}}} = 1 + X$$

In terms of γ this writes:

$$\frac{1}{\frac{1}{\gamma} - 2} = 1 + \frac{1}{\gamma} - 2,$$

which simplifies to

$$\frac{\gamma}{1 - 2\gamma} = \frac{1 - \gamma}{\gamma},$$

and finally:

$$\gamma^2 - 3\gamma + 1 = 0,$$

which has the two solutions

$$\frac{1}{2}\left(3 - \sqrt{5}\right) \approx 0.381966, \quad \frac{1}{2}\left(3 + \sqrt{5}\right) \approx 2.61803.$$

The first one gives, in degrees, 137.51^o..., the second one 232.49^o... (plus two turns).

Some will have recognized in the continued fraction X of our computation, the expansion for $\phi - 1$ where ϕ is the Golden Ratio. Indeed $\frac{1}{X} = 1 + X$ yields the quadratic equation $X^2 + X - 1 = 0$ with only positive solution $\frac{1}{2}(\sqrt{5} - 1) = \phi - 1$. So the continued fraction of the Golden Ratio is:

$$\phi = [1; 1, 1, 1, 1, 1, 1 \dots],$$

the simplest there is! One can show that ϕ (and all the numbers whose continued fraction expansion ends with an infinite sequence of 1's, such as γ for instance) is the most irrational numbers there is: its convergents

$$\frac{1}{1}, \frac{2}{1}, \frac{3}{2}, \frac{5}{3}, \frac{8}{5}, \frac{13}{8}, \frac{21}{13}, \frac{34}{21}, \frac{55}{34}, \frac{89}{55}, \frac{144}{89}, \dots \tag{5}$$

tend to ϕ at the slowest possible rate compared to all other convergents' rate of convergence to their respective real. Intuition for that can be derived when we see (at the beginning of this discussion) that each term a_{k+1} of the expansion is the integer part of $1/r_k$. Since r_k measures in some sense the error at a given step k to be exactly equal to the number x being approximated, the smaller it is, the bigger a_{k+1}. So, if all the $a_k's$ are 1, the smallest they can be, the error to x be rational is at each step as large as it can be.

5 The Fibonacci rule along the van Iterson Diagram

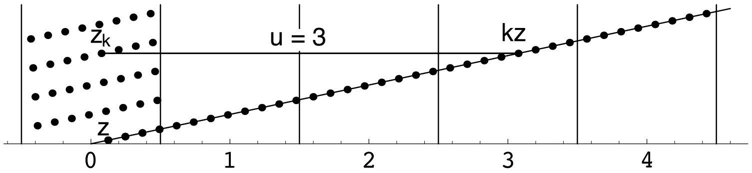

Figure S4: Unrolled cylindrical lattice on a cylinder of circumference 1. The k^{th} point in the lattice generated by $z = (\alpha, G)$ has coordinates $z_k = (k\alpha - u, kG)$ where u, the closest integer to $k\alpha$, represents the number of turns it takes to go from 0 to z_k along the generative spiral ($u = 3$ in the figure).

In this supplementary section we explore in more detail the geometric and number theoretic aspects of the diagram in Fig. 4 of the main text. We start with explaining why arcs of circles are ubiquitous in that diagram. As mentioned in the main text, the (i, j) branch of the van Iterson diagram represents the set of points $z = (\alpha, G)$ such that the Disks i and j in the corresponding lattice are the closest to Disk 0 and are equidistant to it. But as illustrated in the Fig. S4, the centers z_i and z_j of Disks i and j are of the form $z_i = (i\alpha - v, iG), z_j = (j\alpha - u, jG)$ where v (called encyclic number) is the number of turns it takes to go from 0 to z_i on the helix through 0 and z (called the generative spiral). Likewise for u. Let's express now the rhombic condition that z_i and z_j are equidistant to 0:

$$(i\alpha - v)^2 + (iG)^2 = (j\alpha - u)^2 + (jG)^2$$

Expending the squares and regrouping terms involving α and G on one side, the constant on the other:

$$(i^2 - j^2)\alpha^2 + 2(ju - iv)\alpha + (i^2 - j^2)G^2 = u^2 - v^2$$

Dividing by $(i^2 - j^2)$:

$$\alpha^2 + 2\frac{(ju - iv)}{(i^2 - j^2)}\alpha + G^2 = \frac{(u^2 - v^2)}{(i^2 - j^2)}.$$

Finally, the two terms involving α can be completed into a square, yielding an equation of the form:

$$(\alpha + C)^2 + G^2 = R^2$$

where $C = \frac{(ju-iv)}{(i^2-j^2)}, R^2 = \frac{(u^2-v^2)}{(i^2-j^2)} + C^2$. This equation is that of a circle of radius R centered at $(C, 0)$, on the $\alpha-$axis. This algebra computes not only the equations of the branches of the van Iterson diagram, but also the circular boundaries of the regions of different modes: one changes mode when the second closest disk changes. The border of this change occurs when two disks are equidistant to the origin, and an equation as above applies.

In the diagram of Fig. S5, it turns out that, immediately under each region of mode (i, j), there are two regions of modes $(i + j, j)$ and $(i, i + j)$ (Atela et al., 2003), see figure above. This makes intuitive sense: if in the lattice, Points i and j are closest to the reference point 0, then by symmetry, Point $i + j$ is closest to both of them. Traveling down in the (α, G) plane along the branch of the van Iterson diagram in region (i, j) (dashed line in Fig. S5), as one crosses the vertex at the bottom of the branch, the point $i + j$ of the corresponding lattice becomes one of the closest two to point 0. One of the sets of i or j contact parastichies is then replaced by the new

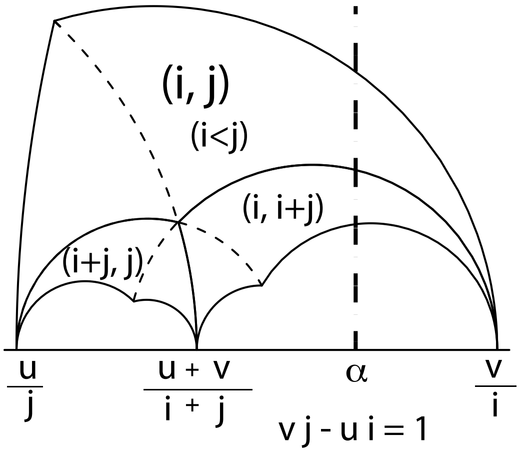

Figure S5: Regions of modes $(i,j),(i+j,j)$ and $(i,i+j)$ are separated by arcs of circles perpendicular to the α-axis. The van Iterson diagram (dashed here) traverse these regions in their middle

one, $i+j$. But which of the two? Remarkably, the choice compatible with the stacking process is always so that one goes from mode (i,j) to mode $(i,i+j)$ (if $i>j$) or $(i+j,j)$ (if $i<j$).

But this is the Fibonacci rule! Take for example $(i,j)=(3,5)$. Then $3=i<j=5$, so the next mode compatible with the stacking process is $(i+j,j)=(8,5)$. More generally, a mode of two consecutive Fibonacci numbers gives rise to a mode with the next two consecutive numbers. The rejected choice yields lattices with the two sets of parastichies winding in the same direction, which is incompatible with the stacking process, as older nearest neighbors are always on the opposite sides of the incoming disk. This explains why, right below branch (i,j) one of the 2 branches $(i+j,j)$ or $(i,i+j)$ of the van Iterson diagram in Fig. 4 of the main text and Fig. S5 is cut.

Traveling down the van Iterson diagram from its top (1, 1) branch, one has to first make a choice of going left in the (2,1) region or right in the (1,2) region - this choice will determine the chirality of the pattern. Say we go left, decreasing of T while varying α to keep the lattice rhombic will lead us down through region of successive Fibonacci modes. While α has to oscillate back and forth to keep the lattice rhombic, it does so with less and less amplitude as it converges to the point $(\gamma,0)$ on the α-axis.

Convergents, revisited. Fig. S5 also shows visually the correspondence between rational approximations of a divergence angle and the parastichy numbers in this cylindrical model. Indeed one can show that the two "foot" points on the α axis of the region of mode (i,j) are $\frac{u}{j}$ and $\frac{v}{i}$ where u,v are such that $vj-ui=\pm1$ and $0<v\leq i, 0<u\leq j$ (see Fig. S5). As a result, if a lattice of divergence angle α is in mode (i,j), $\frac{u}{j}$ and $\frac{v}{i}$ are the best approximation using pieces of size i and j respectively of α (As we know, these best approximation fractions include in particular all the convergents of α). Conversely, if an angle α is between two rationals $\frac{u}{j}$ and $\frac{v}{i}$ where $ui-vj=\pm1, 0<v\leq i, 0<u\leq j$, the lattice given by (α,T) *must* have parastichy numbers (i,j) for *some* range of G: the vertical line for that value of α necessarily crosses the region of mode (i,j). This is a geometric view of the fundamental theorem of phyllotaxis.

6 Fronts, their parastichy numbers and transitions

As stated in the main text and Box 2, a front is, when it first appears, the most recent layer of primordia, directly surrounding the meristem central zone. In the disk stacking model, fronts form a zigzagging line of tangent disks going around the cylinder. This line can be explicitly traced by segments joining the successive centers of tangent disks. Look at the dashed front at disk 14 in Fig. S6A to visualize the simple rules: the line should return to its initial point after one turn around the cylinder, without self-intersection. At each step, the segment traced should go from left to right, and go as high as it can without going higher than the initial point. And, to account for the front being the newest layer of primordia we require that a disk stacked on a front is necessarily higher than all the disks of the front. In Fig. S6A, we traced a horizontal line passing through the center of disk 14 as a guide of how far up we could trace the front. It makes it clear that the center of the next disk, 15, is indeed above that line.

To our knowledge fronts appear first in (Hotton et al., 2006; Atela and Golé, 2007) at this level of generality. However van Iterson (1907) already used "zigzaglinie" that are fronts, but just of "square" lattices, *i.e.* with perpendicular parastichies. He considered these zigzaglinie to be obligatory checkpoints in Fibonacci transitions, and did not use fronts for transitions in between.

Front parastichy numbers The segment in a front is "up" if one goes up by tracing the it from left to right, and similarly for a "down" segment. The *front parastichy numbers* form the pair

$$(\# \text{ of up segments}, \# \text{ of down segments}).$$

If a front is within a region of the configuration where the mode is constant, the pair of front parastichy numbers are equal to the mode. In other words, in the regular case, front parastichy numbers and the regular parastichy numbers are one and the same. For instance, the front at 14 in Fig. S6A has parastichy numbers (4, 5) and it is in the region between disks 1 and 22, where there are 5 (green) parastichies going up ("up-parastichies") and 4 (red) parastichies going down ("down-parastichies"). This is not a concidence: as one goes down a down-parastichy (say 26-21-17-14-9 ...) the first point one hits in the front (14 here) is the upper point of an up-segment (8-14 here). Likewise 20-15-12-8 hits the front first at 12, the top of the up-segment 7-12. This creates a one to one correspondence between down-parastichies, and up segments in the front. Likewise going up an up parastichies (e.g. 5-10-16...), one hits first the lower tip of a down-segment (10 here), creating a one to one correspondence between up parastichies and down segments of the front.

Front transitions. A front can be seen as a succession of V-shaped notches. For instance, in Fig. S6A, the front at 14 is composed of notches 14-9-13, 13-10-6-11 and 14-7-12 and 12-8-14. Stacking a new disk onto a front changes the front. The most common transition is *quadrilateral:* The two older contact neighbors of the new disk (a.k.a. new lateral organ) are located on the opposite wings of a notch, with a fourth disks at the vertex of the notch, separating them. For instance the first new disk after the front at 14 is disk 15, with older contact neighbor, disks 11 and 12. Disk 11 is on the left wing 11-7 of notch 11-7-12 and disk 12 is on its right wing 7-12. These two contact neighbors are separated by, and in contact with disk 7, the bottom of the notch. Disks 15, 11, 7, and 12 together form a quadrilateral, almost a rhombus here since the disks are almost of the same size. The new front at 15 has the same parastichy numbers as the front at 14: the only change in the front is that the down segment 11-7 has been replaced by 15-12, and the up segment 7-12 by 11-15, an operation which incurs no change in the total numbers of up and down segments.

When the size of the disks is reduced, notches open up and the contact neighbors can't be on opposite wings of the notch without violating the stacking rules anymore. (Fig. S6B') Then, the older contact neighbors of the new disk are themselves in contact with one another and on the same side of the notch: the three disks form a triangle. For instance, in Fig. S6A (also B'), the notch 19-16-20 has an angle too wide for the new disk to have contact neighbors 19 and 20, without intersecting 16. The new disk, 23, chooses the two adjacent disks 19 and 16 as contact neighbors, which are both on the flatter wing of the notch.

Sometimes, different parts of the opposite wings of the notch can bend closer to one another and become contact neighbors to the new disk, yielding a pentagon or even a polygon with more sides than 5. This happens when the front is not very regular, or when the ratio d/C is increasing instead of decreasing. In Fig. S6A (and also B"), such a transition occurs at notch 23-26-20-26 of the front at 27. In this transition, the up segments 16-20 and 20-26 are replaced by only one up-segment, 23-28. So the up-parastichy number goes down by one, from 6 to 5.

At a global level, quadrilateral transitions continue building up- and down-parastichies. On the other hand, a triangle transition provokes, as one goes up in the structure, the branching of one parastichy into two, whereas a pentagon transition merges 3 parastichies into two. This can be seen as a 2D version of what crystallographers call dislocations. We can see examples in the next chapter.

7 Local transitions and quasi-symmetric modes

Since the global effect of the transition between Fibonacci modes is so regular, it is tempting to think that the transition is global, while it is due only to an accumulation (with the right number) of local "triangle" transitions. Such transitions can be visible locally. This was studied in details by Beata Zagorska-Marek (Zagorska-Marek, 1985; Wiss and Zagorska-Marek, 2012). An example can be seen in Fig. S7. In such a case, going from a spiral pattern (7, 6) to a pure whorled pattern (7, 7) is quite a change in terms of the divergence angle. The whorled mode is seen as composed of 7 distinct generative spirals (the greatest common divisor of the parastichy numbers), each of them in the mode (1,1). In general, since Bravais 1834, when a pattern (p, q) is observed, one assumes that the number of generative spirals is the greatest common divisor k of p and q: $p = kr$, $q = ks$. Then each generative spiral yields the mode (r, s), and the pattern is interpreted as a $k(r, s)$ modes side by side. Here, the greatest common divisor of 6 and 7 is 1, so it is interpreted as one generative spiral, with a divergence angle of 360 times 6/7. Here with just a local triangle transition, one jumps to the whorled by 7 mode, with 7 generative spiral with a local angle (within each 7 copies) of 360 time 1/2 divided by 7 copies. This is quite a surprising jump. One can thus consider that the description in terms of multiple or single divergence (depending on the common denominator of the parastichy numbers), is useful purely as a pattern description, but meaningless in terms of pattern building dynamics.

In general local transitions are necessarily seen each time the growth index is changed, to accommodate for the different disk sizes. When the transition is slow enough (Golé et al., 2016), one observes the succession of Fibonacci transitions (see Fig. 6 of main article). In such cases the individual transitions are not as visible since they are coherently grouped at the global transitions where the pattern is globally a hexagonal packing, and thus globally regular. When the variation is too quick, the transitions in one direction and another are gathered together in the same smaller time interval (See Fig. S8). It leads to quasi-symmetric modes (Golé et al., 2016). In this article, numerical simulations were done starting from a disk of a given diameter, and piling discks with decreasing size up to a given small size, and a particular speed of decrease. Depending essentially on the speed of decrease, the front would undergo Fibonacci transitions as described in Fig. 5C (main text) for slow speed, and quasi-symmetric for high speed, as show in Fig. S9. That figure also shows how the speed of decrease correlates to the irregularity of the successive fronts.

Such quasi-symmetric modes can be seen in many inflorescences, for instance *Spathypillium*, *Banksia*, corn, peteh... (Douady and Golé, 2017). As a trace of their exceedingly quick decrease of growth index, some irregularity remains and even when the growth index stabilizes, these irregularities induce local transitions. This is most easily seen in *Spathypillium*, Fig. S10, and quite often in corn (*Zea mais*), see Fig. S11 and Fig. S12. But it can stabilize enough to remain perfectly stable and regular, as a rhombic lattice, as in *Banksia*, Fig. S13.

The quasi-symmetry of these inflorescences is easily guessed by looking a the angle of the orthostichies, or third vertical family of contact parastichies. In these cases it is very vertical nearly along the cylinder axis (Fig. S13). If the two numbers are exactly equal, orthostichies are exactly along the cylinder axis. This can be recognized easily in corn, where the row of grains can coil slightly or remain perfectly vertical, while the phyllotaxis goes, depending on the specimen and on the variety, from (2,2) (2,3), (3,3) ... to (5,6), (6,6), this last one showing $(6 + 6) * 2 = 24$ rows of seeds.

The local transitions and the tendency to irregular modes due to fast growth in meristem diameter, to convergence toward quasi-symmetric can be seen in our specimen of corn (Fig. S12), but also generally in cedar male cones (Douady and Golé, 2017), as shown in Fig. S14.

References

Atela, Golé, and Hotton (2003). A Dynamical System for Plant Pattern Formation: A Rigorous Analysis. Journal of Nonlinear Science, 12(6):641–676.

Atela, P. and Golé (2007). Rhombic tilings and primordia fronts of phyllotaxis, preprint.

Debat, V. and David, P. (2001). Mapping phenotypes: canalization, plasticity and developmental stability. Trends in Ecology & Evolution, 16(10).

Douady, S. and Golé, C. (2017). Fibonacci or Quasi-Symmetric Phyllotaxis, Part II : Botanical Observations. Acta societatis botanicorum Poloniae, This special issue.

Gibson, G. and Wagner, G. (2000). Canalization in evolutionary genetics: a stabilizing theory? BioEssays, 22(4):372–380.

Golé, C., Godin, C., and Douady, S. (2020). Cylinder and spiral lattices, interactive geogebra program, https://www.geogebra.org/m/atpsecjr.

Golé, C. (2020). Archimedean spirals, interactive geogebra program, https://www.geogebra.org/m/q5ysr7bvmaterial/feycx5yb.

Golé, C. and Douady, S. (2019). Convergence of a disk stacking process on the cylinder (preprint). http://arxiv.org/.

Golé, C., Dumais, J., and Douady, S. (2016). Fibonacci or quasi-symmetric phyllotaxis. Part I: why? Acta societatis botanicorum Poloniae, 85(4):1–34.

Hall, B. K. (2012). Evolutionary developmental biology. Springer Science & Business Media.

Hotton, S., Johnson, V., Wilbarger, J., Zwieniecki, K., Atela, P., Golé, C., and Dumais, J. (2006). The possible and the actual in phyllotaxis: Bridging the gap between empirical observations and iterative models. Journal of Plant Growth Regulation, 25(4):313–323.

Karpenkov, O. (2013). Geometry of Continued Fractions, volume 26 of Algorithms and Computation in Mathematics. Springer-Verlag.

Maynard Smith, J., Burian, R., Kauffman, S., Alberch, P., Campbell, J., Goodwin, B., Lande, R., Raup, D., and Wolpert, L. (1985). Developmental Constraints and Evolution: A Perspective from the Mountain Lake Conference on Development and Evolution. The Quarterly Review of Biology, 60(3):265–287.

Van Iterson, G. (1907). Mathematische und microscopisch-anatamische studien uber blattstellungen, nebst betraschungen uber der schalenbau der miliolinen gustav-fischer-verlag. G. Fischer: Jena. available online through google books.

Waddington, C. H. (1942). Canalization of development and the inheritance of acquired characters. Nature, 150(3811):563–565.

Waddington, C. H. (1953). Epigenetics and evolution. In Symp. Soc. Exp. Biol, volume 7, pages 186–199.

Waddington, C. H. (1961). Genetic assimilation. Advances in genetics, 10:257–293.

Wagner, A. (2005). Robustness and Evolvability in Living Systems. Princeton University Press.

Wiss, D. and Zagorska-Marek, B. (2012). Geometric parameters of the apical meristem and the quality of phyllotactic patterns in Magnolia flowers. Acta Societatis Botanicorum Poloniae, 81:203–216.

Yamagishi, Y. and Sushida, T. (2017). Spiral disk packings. Physica D: Nonlinear Phenomena, 345:1 – 10.

Zagorska-Marek, B. (1985). Phyllotactic patterns and transitions in Abies balsamea. Canadian Journal of Botany, 63:1844–1854.

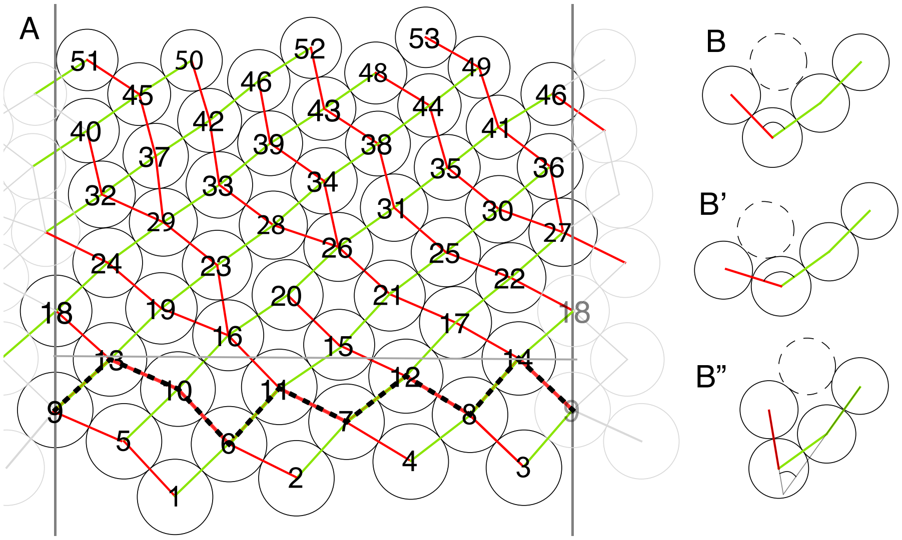

Figure S6: **Transitions and parastichies.** (A) To build the front at 14 (dashed), start at disk 14, and proceed from left to right, joining centers of tangent disks, going as high as you can, but staying below 14 (indicated by a horizontal line). From 14, you must go down to 9, as 18 is too high. You can then go to 13, as it is lower than 14, but then you must go down to 10, as 19 is higher than 14... This front has 4 (green) up segments and 5 (red) down segments, so its front parastichy numbers are (4, 5). This corresponds to the mode (5, 4) in the region between points 1 and 22: there are 5 (green) up-parastichies and 4 (red) down-parastichies here. At disk 23, there is a triangle transition: the angle at the notch 19-16-20 is greater than 120^o so disk 23 can't have both disks 19 and 20 as older contact neighbors: it chooses disks 19 and 16 instead, as they form the flatter wing of the notch (see also (B')). This results in the addition of the extra up-segment 19-23 to the front, which has now parastichy number (5, 5). Note how the red parastichy through 6, 11, 16 forks into two (through 19 and through 23) because of this triangle. At disk 28 there is a pentagon transition: the tips 23-16 and 20-26 of the wings of the notch 23-16-20-26 form an angle less than 60^o (as in (B")). This decreases the front's up-parastichy number by 1: the two up segments 16-20 and 20-26 of the notch are replaced by the single 23-28. Correspondingly, ignoring the triangles on either sides, the 3 red parastichies 6-11-16, 12-15-20, 17-21-26 can be interpreted as merging into the two at 23-29 and 28-33. (B) Quadrilateral transition, the most common. The notch angle is in a range of about $60^o - 120^o$. (B') A triangular transition: the notch angle is larger than 120^o and the new disk can't reach both sides of the notch without intersection. The new disk goes to the flatter side of the notch, to minimize height, as prescribed by the stacking rules. (B") Pentagon transition: the angle indicated is less than 60^o but the notch angle is greater than 60^o, and less than 120^o.

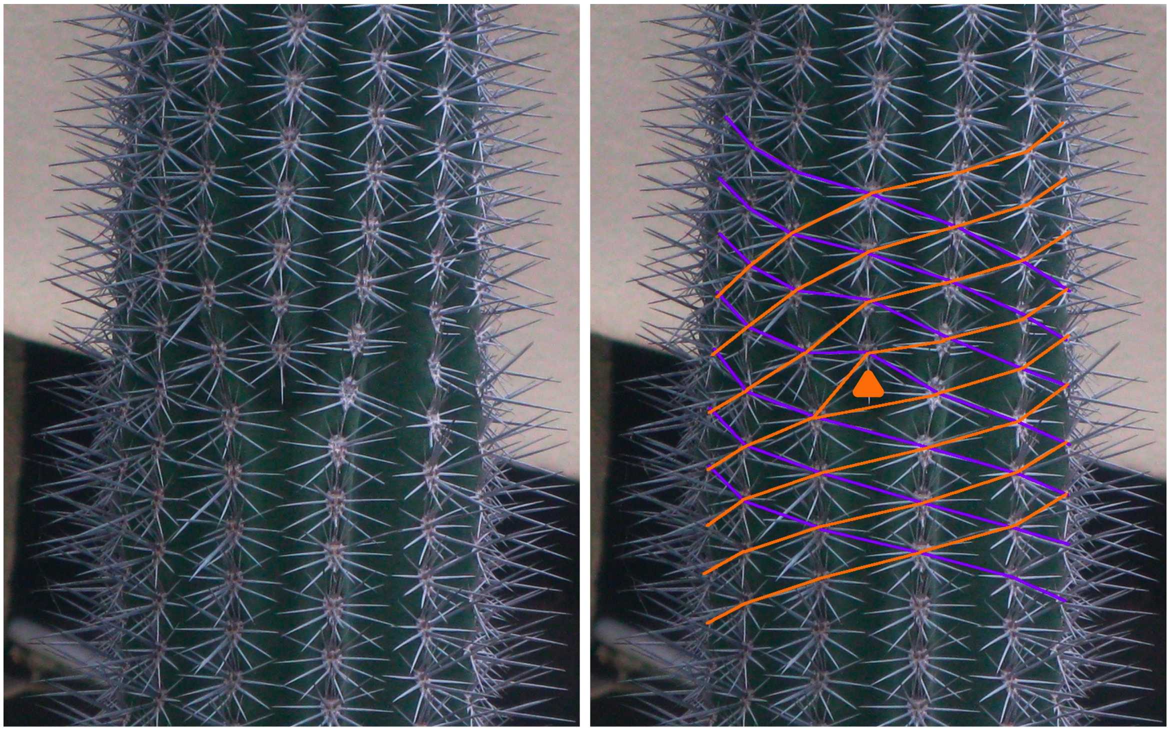

Figure S7: Detail of an elongated cactus . The vertical orthostichies indicate near rational divergences. In the middle, there is a local triangle transition from (7,6) to (7,7). original picture on the left, drawn on the right.

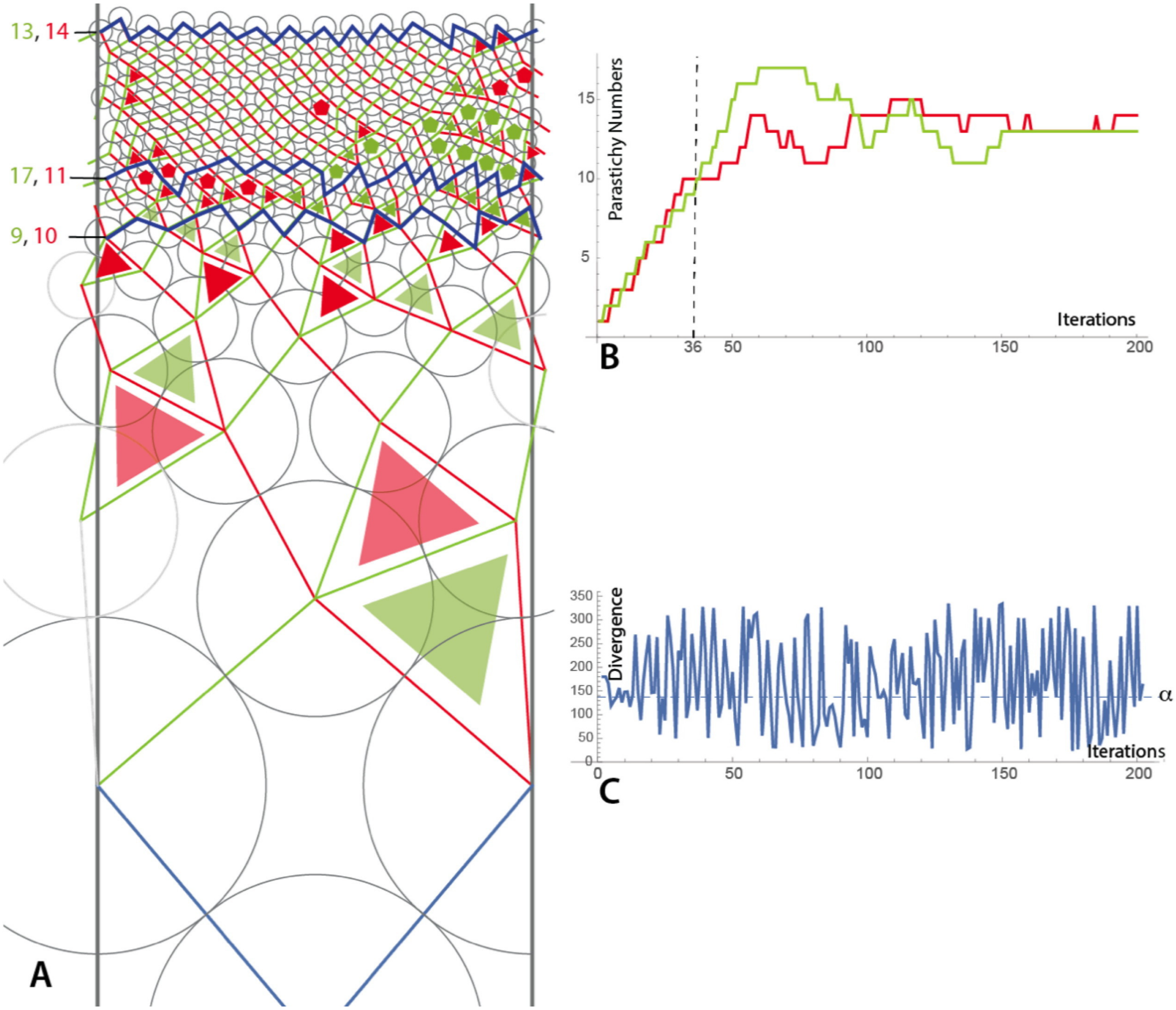

Figure S8: Simulation of a very quick decrease of the size of the disks being stacked, followed, after 36 disks, by stacking of disks of constant size. (A) the unrolled cylinder with the disks stacked. The transitions, necessary because of the decreasing radius, occur in both up and down segments in the same time interval. (B) This leads to a quasi-symmetric number of spirals during the transition. After the size is stabilized (dashed line), the number fluctuates widely but converge toward quasi-identical numbers. (C) during all his process, the divergence is widely fluctuating with no visible meaning.

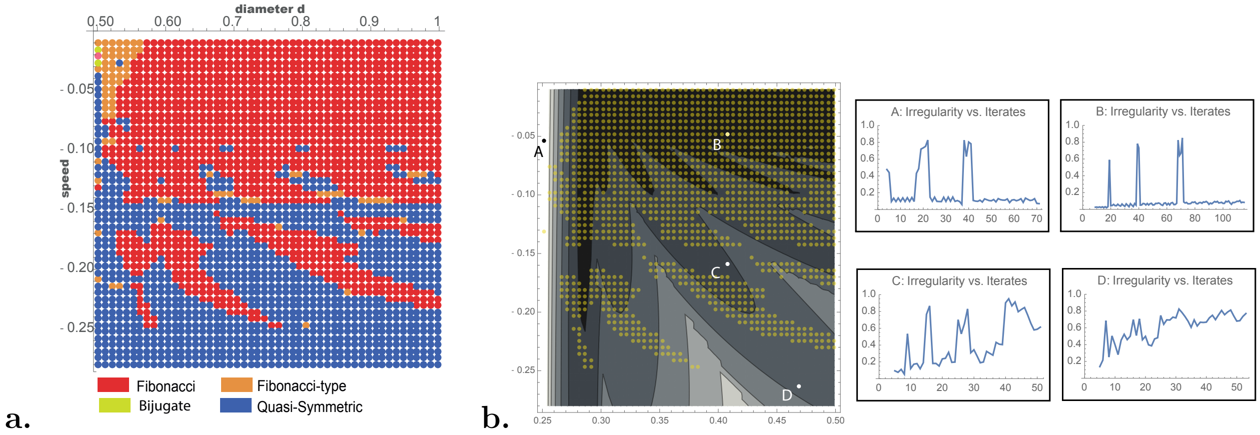

Figure S9: **a.** Results of 2500 simulations, with initial disk size and speed of decrease of the size as parameters (from (Golé et al., 2016)). The result is classified as being true Fibonacci, with transitions as described in Fig. 5C of the main text, Fibonacci type (if the last front is Fibonacci, but the transitions may include pentagons)

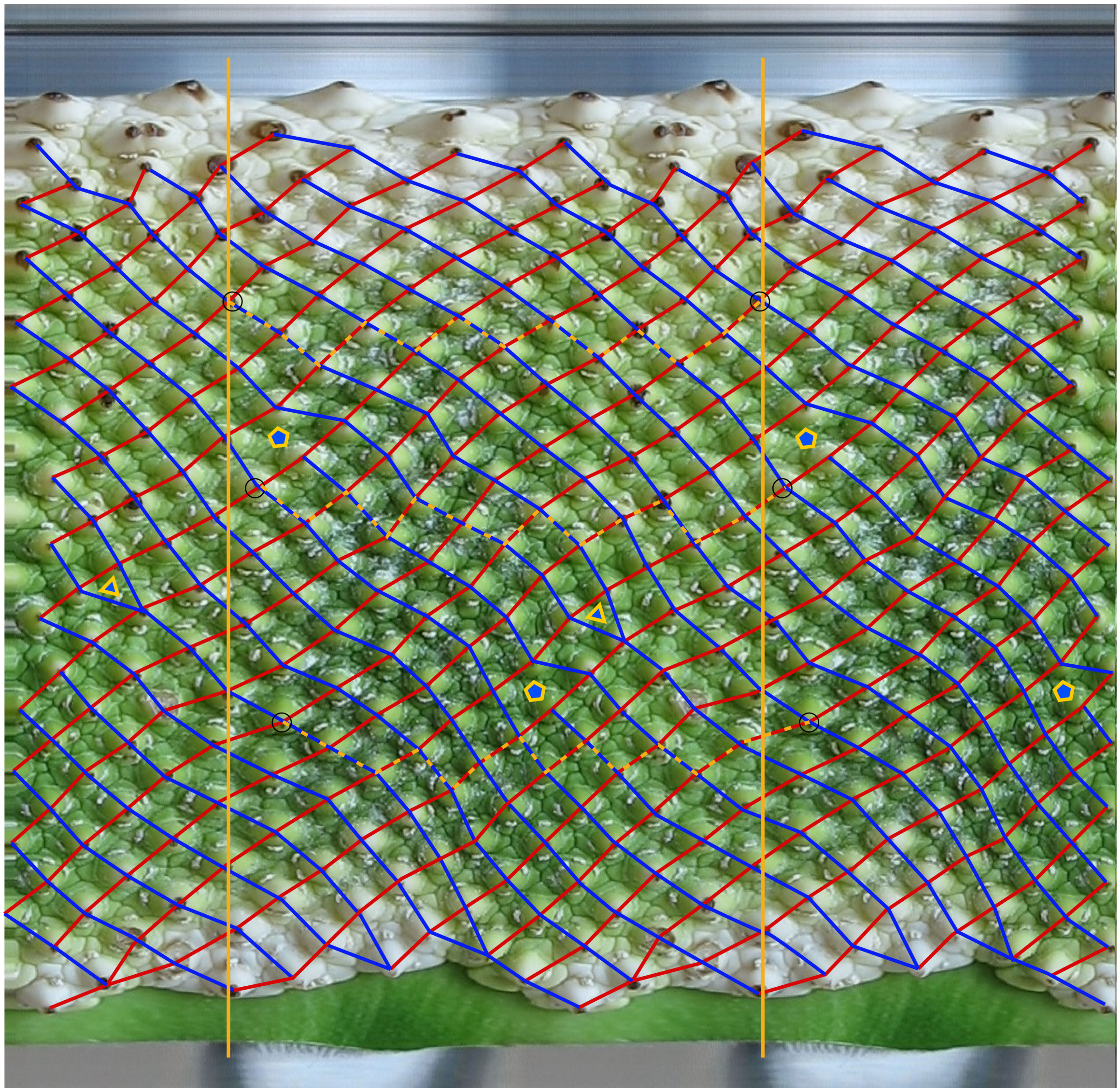

Figure S10: Inflorescence of a *Spathiphyllium*. This inflorescence has been numerically unrolled by turning it in front of a camera, and the central line has been gathered to form a time “reslice” or a horizontal kinetograph, showing a unrolled projection of the inflorescence cylinder. A period of rotation is shown by the two vertical orange lines. In this inflorescence, one can see after an abrupt transient a (6, 7) front, underlined by orange dashes. Then the disappearance of a blue contact parastichy leads to the disappearance of a red step in the front, and a (6, 6) mode. But it is quickly followed by a blue triangle transition, making a red step reappear and a new blue parastichy, back to (6, 7), as is common in the convergence of irregular pattern toward a rhombic tilling (Golé and Douady, 2019)). Finally, a last pentagon transition leads to the symmetric (6,6) pattern.

Figure S11: In corn, the phyllotaxis is not visible at first sight, due to two phenomena, the first one is that each primordium gives rise to two horizontal seeds, the second that the large increase in radius enlarges the seeds horizontally. From a typical corn cob (left), one can then unroll it numerically (middle), as described in Fig. S10, and to visually compensate the lateral growth, compress it considerably in width (right). Then the pairs of seeds start to be easily recognised as single units.

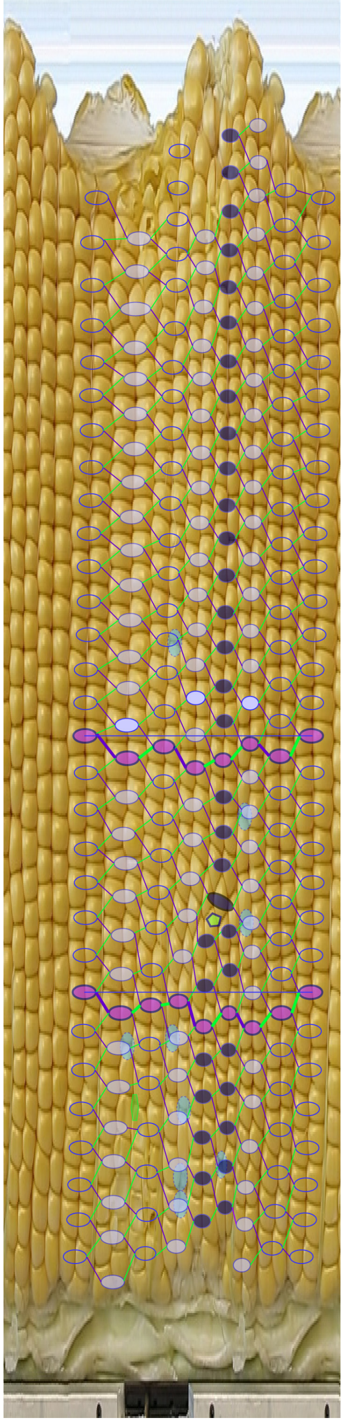

Figure S12: Once the rescaling of Fig. S11 is done, one can analyse the pattern. Another difficulty in corn is that not all the pistils give rise to a fully developed seed (abortion). This leave some empty space in the cob that is filled by the surrounding expanding grains. Such abortions, if not too numerous, can be easily be guessed by enforcing a pairs of seeds everywhere (light blue ovals). Then each primordium can be linked with its two older contact neighbors, here up in green and down in purple. Some quasi-vertical orthostichies have been highlighted for visibility. This particular corn cob, after a complex beginning, still show near the bottom a Fibonacci (3, 5) phyllotaxis, as shown by the underlined front. Then there is a pentagon transition, resulting in the disappearance of a purple step, so a green transverse parastichy, and by consequence one (darker) orthostichy. The upper front shows indeed a normal stable quasi-symmetric (3, 4) phyllotaxis, usual with corn cobs.

Figure S13: Inflorescence of a *Banksia* ("Giant Candles" from Royal Botanical garden of Melbourne). It goes quickly from a normal (2,3) mode to a regular quasi-symmetric (7,8). The slight difference between the two numbers of parastichies is visible in the slight tilt of the orthostichies.

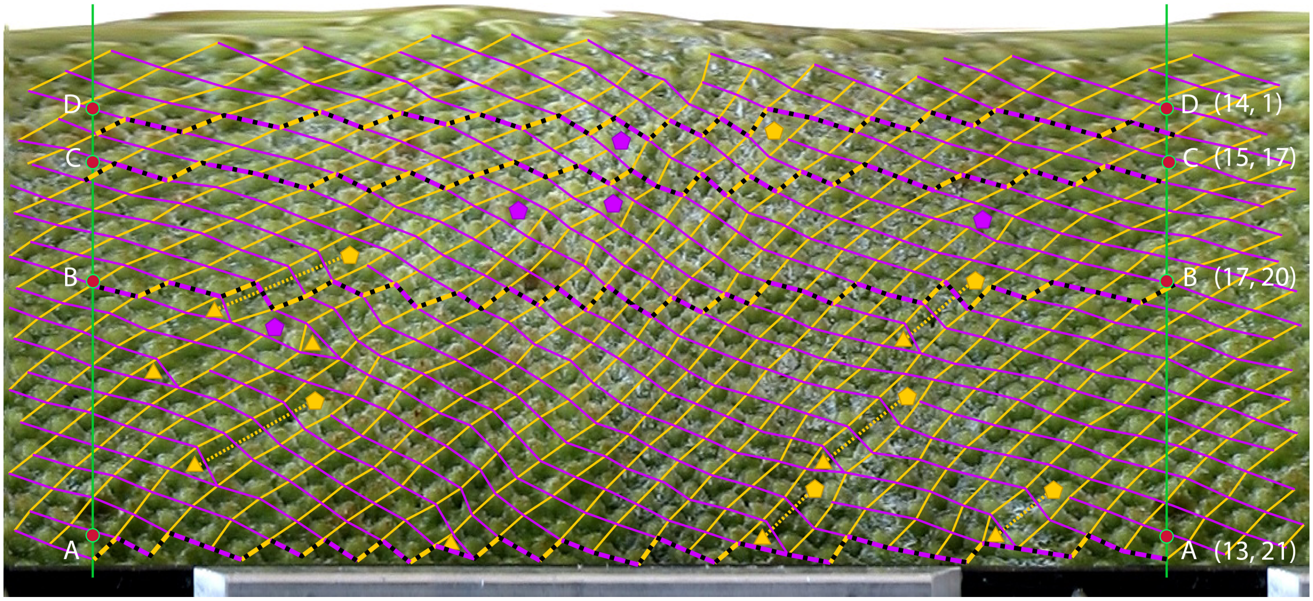

Figure S14: An unrolled cedar male cone. It start from a Fibonacci (13,21) pattern in A (34 orthostichies), that grows quickly to (16,21) (37 orthostichies) with three (yellow) triangle transitions. But these triangles are followed by pentagon transitions, making pairs, a way to reduce the irregularity of the pattern (Golé et al., 2016). . With some isolated local transitions, it reaches a more symmetric (17, 20) in B (still 37 orthostichies), to gradually reduce it diameter, inducing only pentagon transitions, to more quasi-symmetric modes (15, 17) in C (32 orthostichies) and (14,16) in D (30 orthostichies).